

Rapid Update, Flexible, and Advanced Scanning Concepts Demonstrated by the NSSL Advanced Technology Demonstrator Phased Array Radar in CY24

Lead Author: Addison Alford¹

Contributors: Charles Kuster¹, Terry Schuur^{2,1}, Anthony Reinhart¹, Caden Berry^{2,1}, Emily Blumenauer^{2,1}, Jami Boettcher^{2,1}, Jacob Carlin^{2,1}, Kris Tuftedal^{2,1}, Arthur Witt¹, Noah Boeckman^{2,1}, Chris Curtis^{2,1}, Robbie Estes^{2,1}, Eddie Forren^{2,1}, Stephen Gregg^{2,1}, Larry Hopper¹, Igor Ivić¹, Rakshith Jagannath^{2,1}, Gerald Kunkle¹, Rafael Mendoza¹, Feng Nai^{2,1}, Patrick Servello^{2,1}, Chad Smith¹, Sebastián Torres^{2,1}, David Warde^{2,1}, Danny Wasielewski¹, Felicia Woolard¹, Allen Zahrai^{2,1}, and Noah Zemlin^{2,1}

¹NOAA/OAR/National Severe Storms Laboratory; Norman, OK; ²Cooperative Institute for Severe and High-Impact Weather Research and Operations, University of Oklahoma; Norman, OK

Date of Submission: February 2025

Date Accepted for Publication: March 2025



U.S. Department of Commerce
National Oceanic and Atmospheric Administration
Office of Atmospheric Research
National Severe Storms Laboratory

Contents

List of Figures	3
List of Tables	6
1. Executive Summary	7
2. Background and Motivation	8
2.1 Phased Array Radar at NSSL	8
2.2 History of ATD Data	11
3. Data Collection Priorities in CY24	11
3.1 Scan Designs in CY24.....	11
3.1.1 Traditional and Non-Traditional Scanning Strategies	13
3.1.2 Linear Depolarization Ratio.....	14
3.1.3 A Brief Review of Engineering Scan Designs	15
3.2 Observing Objectives.....	16
3.2.1 On the Operational Benefits of PAR.....	16
3.2.2 Fundamentals of Severe Weather Research	16
3.2.3 Radar Polarimetry	17
3.2.4 Engineering Demonstration	17
4. CY24 Dataset Overview	17
5. Demonstrating the Benefits of PAR in CY24	18
5.1 Potential Operational Benefits.....	18
5.1.1 Rapid-Update Low-Level Data.....	18
5.1.2 Volumetric Updates.....	22
5.2.3 Introducing Flexible, Non-Traditional Scanning	26
5.2 Severe Weather Observations	28
5.2.1 A Non-Tornadic Mesovortex	29
5.2.2 Toward Precipitation Estimation	32
5.3 Dual-Polarization Measurements	33
5.4 Advanced Engineering Concepts.....	35
5.4.1 Assisting with Calibration Efforts	35
5.4.2 Assisting with Adaptive Scanning R&D	38
6. Discussion	38
6.1 Potential Operational Benefits Demonstrated by the ATD	38
6.2 A Flexible and Adaptable Solution?	40
6.3 Moving into CY25.....	41
7. Acknowledgements	41
8. List of Acronyms	42
9. References	42

List of Figures

Figure 1. A conceptual model of Adaptive Focused Observations with PAR is shown. In the image, a PAR antenna faces a supercell thunderstorm producing heavy rain, hail, and a tornado. Possible PAR beam positions are shown by the circles. Gray circles indicate inactive beam positions that are in the clear air around a supercell and do not contain significant weather echo. The orange circles indicate active beam positions in the directions of the supercell and contain significant weather echo.9

Figure 2. Images of the (a) SPY-1A PAR during its dismantle in 2016 and (b) the ATD PAR after its installation in 2018. Images are courtesy of NSSL. In (a), the SPY-1A antenna sits atop the radar tower. The blue radome sits on the ground after it had been removed to dismantle the antenna. In (b), the ATD antenna face is shown, sitting beneath the radome..... 10

Figure 3. The elevation angles of the Supercell scanning strategy for supercells <50 km from the ATD for 2024 with 15 elevation angles (a) and 2023 with 19 elevation angles (b) are shown. In the figure, the elevation angle coverage in the low levels is very similar. In the mid-levels, the 2024 scanning strategy has reduced coverage in favor of redistributed coverage in the upper levels to monitor for upper-level precursor signatures such as hail growth..... 12

Figure 4. A time series (time increases toward the bottom of the figure) of Doppler velocity (shown for context) and correlation coefficient from ATD (left) and KOUN (right) on 28 April 2024. The subpanels each show ρ_{HV} as a function of time at the 0.5° elevation. In the ATD data, a TDS appears at 0154:09 UTC. The same TDS does not appear until 0155:06 UTC in KOUN data. Note that there are some regions of errors associated with an experimental dealiasing scheme in the ATD Doppler velocity plots.20

Figure 5. A time series (time increases toward the bottom of the figure) of correlation coefficient from ATD (left) and correlation coefficient and Doppler velocity from KOUN (right) on 20 May 2024. The subpanels each show ρ_{HV} as a function of time at the 0.5° elevation. In the ATD data, a TDS appears at 0235:25 UTC. The same TDS does not appear until 0236:16 UTC in KOUN data. The aliased Doppler velocity data from KOUN are shown for context.....21

Figure 6. A time series (time increases toward bottom) of three-dimensional isosurfaces of “normalized rotation” computed in GR2Analyst. On the left, ATD volumes of normalized rotation are shown (red is cyclonic). On the right, KTLX volumes are shown. In the figure, the mesocyclone (indicated by the red isosurfaces) are disorganized in the initial ATD and KTLX volumes near 2107 UTC. The ATD, using just over 1-minute volume updates, captured the volumetric evolution, organization, and intensification of the mesocyclone prior to a confirmed tornado occurring at 2110 UTC. KTLX, on the other hand, required about 6 minutes to capture a full volume. “VST” in the figure refers to the radar “volume start time.”24

Figure 7. A time series (time increases toward the bottom of the figure) of K_{DP} from ATD

(left) and KTLX (right) on 15 August 2024. The subpanels each show K_{DP} as a function of time at the 3.7° and 3.1° elevation surfaces from the ATD and KTLX, respectively. In the ATD data, two periods of intensification of the K_{DP} cores are observed. In the KTLX data, the periods of intensification are not resolved.26

Figure 8. A pseudo-RHI at 280° azimuth is shown reconstructed from the 0424:09 UTC volume scan from KOUN. In the left column (panels a and b), PPIs of (a) radar reflectivity and (b) Doppler velocity show a small MCS to the west of KOUN. The dashed black line shows the location of the pseudo-RHI, which is taken through a region of high reflectivity and on the northern side of a region of intense inbound Doppler velocities associated with a small bowing segment. In the right column, the pseudo-RHI (c) reflectivity (also indicated as Z_H), (d) Doppler velocity (also indicated as V), (e) Z_{DR} , and (f) ρ_{HV} are shown from top to bottom.28

Figure 9. A true RHI at 280° azimuth is shown taken at 0428:11 UTC by the ATD. In the left column (panels a and b), PPIs of (a) radar reflectivity and (b) aliased Doppler velocity show a small MCS to the west of the ATD. The dashed black line shows the location of the pseudo-RHI, which is taken through a region of high reflectivity and on the northern side of a region of intense inbound Doppler velocities associated with a small bowing segment. In the right column, the true RHI (c) reflectivity (also indicated as Z_H), (d) Doppler velocity (also indicated as V), (e) Z_{DR} , and (f) ρ_{HV} are shown from top to bottom.28

Figure 10. The evolution of a non-tornadic mesovortex from 2 May 0550:22 to 0552:34 UTC is shown. In panels (a), (c), (e), and (g), Doppler velocity is shown. In panels (b), (d), (f), and (h), K_{DP} is shown. Initially at 0550:22 UTC (a and b), the mesovortex in the figure is relatively compact. The K_{DP} drop behind the main convective line and low-level maximum in K_{DP} within the convective line begins primarily in the next time step at 0550:54 UTC (c and d). The mesovortex subsequently broadens in area coinciding with the enhancement of the K_{DP} drop behind the convective line and intensification of the local K_{DP} maximum in the convective line at 0552:02 UTC (e and f) and 0552:34 UTC (g and h). The data are shown at 0.5° elevation.31

Figure 11. Dual-polarization data from the 2 May 0557:33 UTC PPI is shown, highlighting the mature presentation of a non-tornadic mesovortex. From top left to bottom right, panels of (a) radar reflectivity, (b) Doppler velocity), (c) SW, (d) Z_{DR} , (e) K_{DP} , and (f) ρ_{HV} are shown. The inset in (b) zooms in on the localized maxima in Doppler velocity within the broader mesovortex structure. Several maxima in the K_{DP} field are also indicated to bring attention to the near-co-location and possible relationship between the Doppler velocity and K_{DP} maxima.32

Figure 12. Composite radar-based QPE retrievals (y-axes) from (a) KOUN and (b) ATD are compared to 5-minute rain gauge observations (x-axes). The dashed one-to-one line indicates perfect agreement. The dots indicate observation comparison points and the color-filled contours indicate the density of those points according to the colorbar. In (a), KOUN QPE versus gauge-observed rainfall points are shown scattered around the one-to-one line with substantial spread, particularly above 0.1 inches. Comparatively, the ATD versus gauge observations in (b) are much less scattered and are more concentrated along the one-to-one line, particularly for higher rainfall measurements. The inset text in the figures indicates that each radar observed 885

individual 5-minute increments over the five cases sampled. KOUN and ATD QPE retrievals had mean absolute errors of 0.03 and 0.02 inches, RMSEs of 0.053 and 0.0376 inches, and permutation Pearson r test statistics of 0.75 and 0.86 (both statistically significant with p-values of 0.0001), respectively. The statistics support that the ATD performed better in terms of QPE for the five cases contributing to this composite analysis.33

Figure 13. Dual-polarization data from the 24 September 2334:01 UTC PPI is shown, highlighting hail signatures in a severe storm to the northeast of the ATD. From top left to bottom right, panels of (a) radar reflectivity, (b) Doppler velocity, (c) SW, (d) Z_{DR} , (e) LDR (taken at 2333:55 UTC), and (f) ρ_{HV} are shown. Several distinct reflectivity maxima are indicated in (a) with values upwards of 65 dBZ. In the Z_{DR} field (d), a region of near or less than 0 dB is indicated that is very likely associated with a region of hail as well as differential attenuation. The same region is highlighted in LDR (e), which shows values near -15 dB (suggesting the presence of hail), with small isolated regions approaching -12 dB. The independent information gained from LDR likely adds value and context to the “standard” dual-polarization observations in terms of evaluating hail size, as discussed in the text.34

Figure 14. A time series for hail reports is compared to the ATD time series of (a) reflectivity and (b) LDR. The reflectivity and LDR time series are taken by only considering areas where reflectivity exceeded 55 dBZ. The black lines in each figure indicate the median value of reflectivity and LDR. The darker shading around the median line indicates the 25th to 75th percentile ranges. The lighter shading around the median indicates the 10th to 90th percentile ranges. The time series shows several peaks in reflectivity and LDR: a sharper peak near 23:07 UTC and a broader peak near 23:45 UTC. At those times, maximum hail sizes from reports were near 70 mm and 65 mm, respectively. The median, 75th, and 90th percentile values of reflectivity were near 60, 65, and 68 dBZ at both hail size peaks. However, LDR median, 75th, and 90th percentile values of LDR were near -20, -17.5, and -14 dB in the first peak and -19, -18, and -16 dB near the second peak, indicating utility in the independent information gleaned from LDR in hail sizing via radar observations.35

Figure 15. From left to right, fields of reflectivity, differential reflectivity, and differential phase for data collected with the ATD using pencil beams (a-c) and spoiled transmit beams with 5 simultaneous receive beams (d-i). Data in the (d-f) were calibrated using pre-existing correction factors derived for pencil beams only, while data in the (g-i) were calibrated using experimental weather data collected on 5 July 2024 1439:14 UTC.36

Figure 16. Magnified fields of reflectivity (a), differential reflectivity (b), correlation coefficient (c), and differential phase (d) from corrected spoiled beam data. The figure shows data collected by spoiled transmit beams to highlight the discontinuities discussed in the text. One group of simultaneously received beams is denoted between the white lines in (c).37

List of Tables

Table 1. Storm-type event counts collected by the ATD in CY24. The total number of cases summed across all categories is 45. 18

Table 2. A list of all cases is shown with the case times and the general storm type observed. The fourth through eighth columns show the scan (VCP) date and time, the name of the scan, the ATD sector date and time, and the left (L) and right (R) edges of the ATD's sector. The information in these columns is color-coded according to changes in the VCP and sorted by time according to changes in the scanning strategy.45

1. Executive Summary

The National Oceanic and Atmospheric Administration (NOAA) National Severe Storms Laboratory (NSSL) has an extensive history of being a leader in weather radar research. Phased array radar (PAR) for weather observation has been studied at NSSL since the early 2000s. In the mid-2010s, NSSL acquired the dual-polarization Advanced Technology Demonstrator (ATD) PAR to examine the feasibility of dual-polarization remote sensing measurements with a planar PAR antenna. In the early 2020s, a robust dual-polarization weather calibration was achieved on the ATD. This achievement has enabled the use of the ATD to demonstrate the operational possibilities of dual-polarization PAR. This is important as the National Weather Service (NWS) considers its next operational radar fleet to be installed in the 2035-2040 timeframe.

To demonstrate the potential operational benefits of PAR, the ATD was leveraged in calendar year 2024 (CY24) to collect more than 145 hours of meteorological data across 45 separate cases. Observations from these cases included tornadic and non-tornadic supercells, mesoscale convective systems, severe and non-severe multicellular convection, downbursts, winter weather events, and clear air echoes. Many of the potential operational benefits elucidated by these cases focus on the rapid, one-minute volumetric and sub-one-minute low-level updates achieved by electronic beam steering. Such rapid, low level and volumetric updates afford for earlier detection of dual-polarization signatures related to severe hazards, the better depiction of precursor signatures aloft to near-surface hazards, and the potential for current and future algorithms requiring high spatiotemporal measurements for optimal performance.

PAR not only enables rapid low-level and volumetric updates that mimic current operational scan designs, but also can be leveraged to scan the atmosphere in flexible and adaptable manners that are not practical to implement on mechanically driven radar systems using parabolic antennas. In CY24, improvements to the ATD's user interface, the implementation of new transmission modes, and the development of novel scanning algorithms resulted in further demonstrating the potentials of PAR. One-second vertical scans (range height indicators) were often employed between traditional radar volume scans, capturing high resolution details about the vertical structure of severe convection. New transmission modes were designed and enabled on the ATD to provide independent information that can extend the utility of dual-polarization estimates of hail size. A new version of adaptive scanning was developed and initially tested in late CY24 to automatically detect beam positions that contain significant weather echo, further reducing scan times and focusing radar resources onto targets of interest. In this report, we review the efforts in CY24 to demonstrate the operational utility of PAR, the critical research and development efforts underway afforded by observations from the ATD, the potential benefits of varying transmission modes enabled by PAR, and the advanced techniques being developed to reduce scan times on the ATD.

2. Background and Motivation

The National Oceanic and Atmospheric Administration (NOAA) National Weather Service (NWS) currently operates a network of 159 S-band (10 cm wavelength) dual-polarization¹ weather radars called the Weather Surveillance Radars - 1988 Doppler (WSR-88Ds; Crum and Alberty 1993; Doviak et al. 2000). Many of the components of the WSR-88Ds are aging, which has prompted the NWS to consider options for its next radar fleet (NOAA 2024). The Radar Next Program will complete an Analysis of Alternatives (AoA) to identify candidate technologies to be considered for the next operational radar fleet.

2.1 Phased Array Radar at NSSL

Phased Array Radar (PAR) technology has been employed for military applications for decades. In the early 2000s, the NOAA National Severe Storms Laboratory (NSSL) acquired a SPY-1A PAR (donation by the U.S. Navy) with which NSSL began testing the feasibility of using single-polarization PAR for weather applications. Through datasets collected with the SPY-1A, the benefits of PAR for weather observations were explored including advanced beam forming capabilities (e.g., Zrnić et al. 2007), rapid update radar volumes to diagnose rapidly evolving severe weather (e.g., Heinselman et al. 2008; Newman and Heinselman 2012), and the benefit of assimilation of PAR data in numerical weather prediction models (e.g., Stratman et al. 2020). In addition, data from the SPY-1A was leveraged in the NOAA Hazardous Weather Testbed (HWT) to show that NWS forecaster decision making in issuing tornado warnings, for example, was improved by PAR data (Heinselman et al. 2012, 2015).

Through exploration of PAR via the SPY-1A, additional benefits of PAR were elucidated. An algorithm for Adaptive Focused Observations (AFO) was implemented on the SPY-1A (Torres et al. 2016), which involved automatically deactivating electronically scanned beam positions when no significant weather return exists (e.g., Figure 1) and routinely checking to determine if inactive beams should be re-enabled. AFO can theoretically be implemented by any weather radar including a rotating, parabolic antenna weather radar like the WSR-88D. However, the utility of this type of adaptive scanning technique is impractical on radars like the WSR-88Ds due to the time required to accelerate and decelerate the radar antenna to focus on a weather target that encompasses a small portion of the radar coverage area as shown in the example in Figure 1. Nevertheless, the WSR-88Ds do employ one form of AFO: the Automated Volume Scan Evaluation and Termination (AVSET) technique. AVSET eliminates

¹ Note in this document, we use the term “dual-polarization,” but note that “polarimetric” may also be used in most instances interchangeably.

elevation angles above 5° when no significant weather echo is present. With PAR's ability to near-instantaneously change beam positions through electronic beam steering, AFO can be used to not only eliminate entire elevation angles from a scanning strategy, but also can be used to selectively scan in all directions within a PAR antenna's field of view. Hence, AFO is *most* beneficial and practical to implement on a PAR.

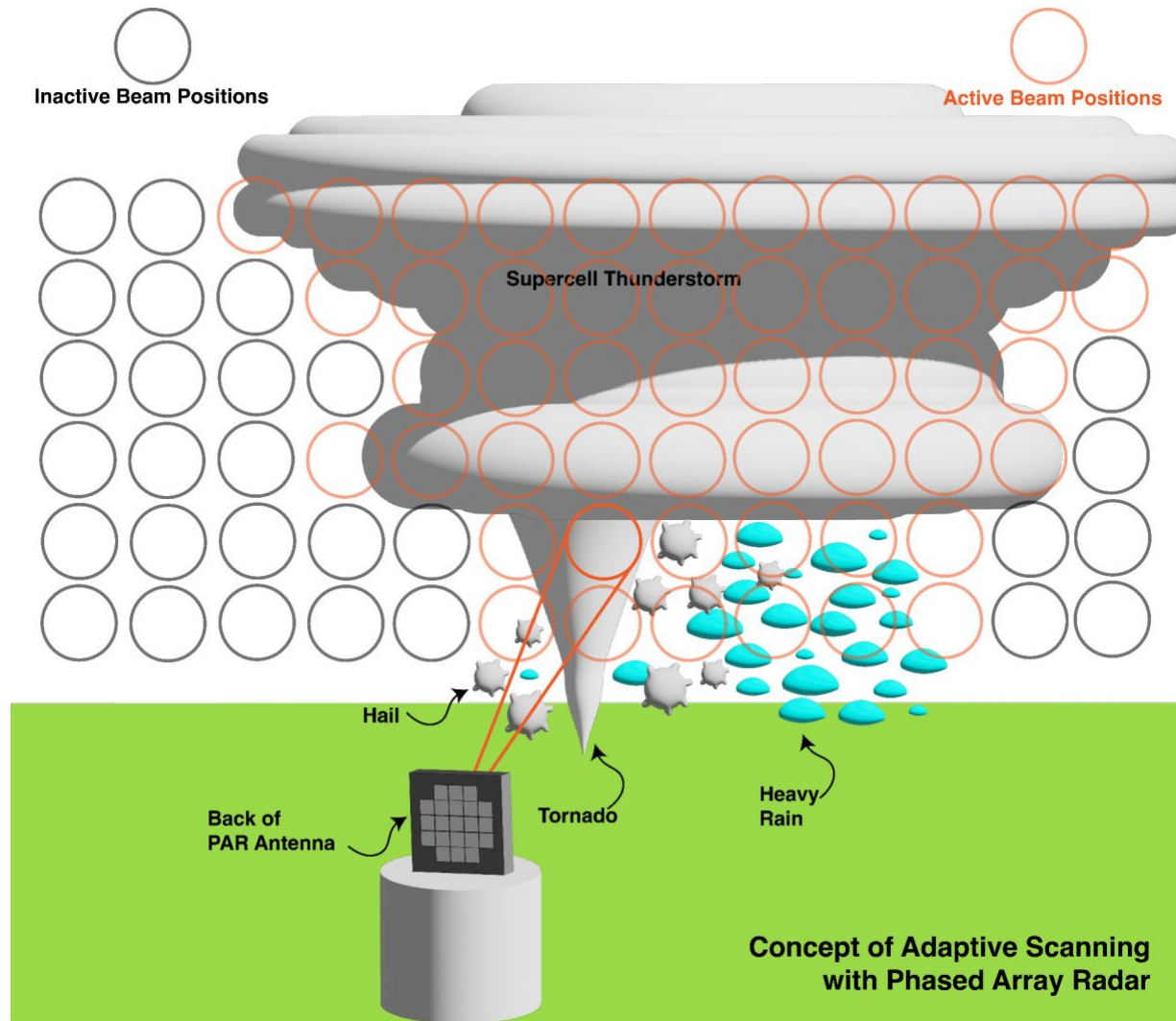


Figure 1. A conceptual model of Adaptive Focused Observations with PAR is shown. In the image, a PAR antenna faces a supercell thunderstorm producing heavy rain, hail, and a tornado. Possible PAR beam positions are shown by the circles. Gray circles indicate inactive beam positions that are in the clear air around a supercell and do not contain significant weather echo. The orange circles indicate active beam positions in the directions of the supercell and contain significant weather echo.

While many lessons were learned from the SPY-1A antenna, the adoption of dual-polarization on the WSR-88Ds prompted NSSL to consider dual-polarization implementation on a PAR system. As such, the SPY-1A was decommissioned (Figure 2a) in favor of the new Advanced Technology Demonstrator (ATD) PAR (Figure 2b) in the

mid 2010s. The ATD was the first S-band, dual-polarization PAR built for weather observation. Its primary goals are as follows:

1. Evaluate the feasibility of dual-polarization measurements using a planar array PAR system.
2. Demonstrate functionality using *one side* of a four-faced, non-rotating PAR concept.
3. Serve as a primary research and development tool for NSSL to advance concepts including, but not limited to, novel PAR beam forming, adaptive scanning techniques, signal processing, and fundamental weather observation.

The ATD has a 90° field of view relative to the direction of the antenna face and can be repositioned to scan a sector of interest.

A fundamental question addressed by the ATD was the combination of dual-polarization and PAR technologies. Upon steering an electronically scanned beam off broadside (i.e., the direction normal to the PAR antenna face), the transmitted horizontal and vertical polarized waves cross-couple (i.e., are no longer orthogonal), which ultimately biases the dual-polarization data as a function of beam steering angle. A calibration tower placed near the ATD was used to determine the biases induced in both the transmitted power and phase as a function of beam steering angle, and correction factors were developed (Ivić et al. 2020, 2023). As a result, a robust calibration for the ATD was achieved in the early 2020s, demonstrating that dual-polarization PAR is achievable.

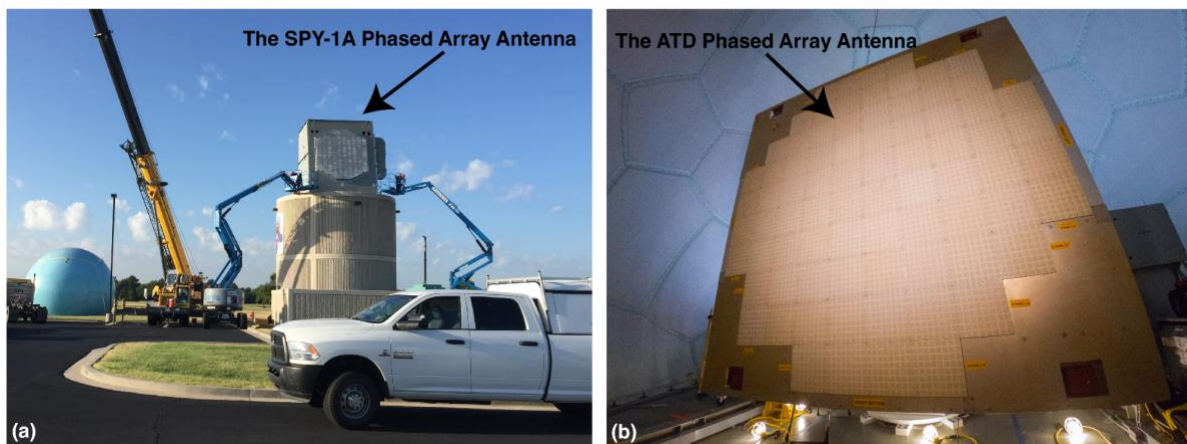


Figure 2. Images of the (a) SPY-1A PAR during its dismantle in 2016 and (b) the ATD PAR after its installation in 2018. Images are courtesy of NSSL. In (a), the SPY-1A antenna sits atop the radar tower. The blue radome sits on the ground after it had been removed to dismantle the antenna. In (b), the ATD antenna face is shown, sitting beneath the radome.

2.2 History of ATD Data

The ATD reached initial operating capability in April 2021 (Torres and Wasielewski 2022). Although several initial datasets were collected in 2021 and 2022, the majority of weather data collected by the ATD began in 2023. Discussed in Alford et al. (2024), the ATD was used to collect more than 150 hours of data in a wide variety of severe and non-severe weather events that impacted central Oklahoma. The primary goal of the ATD in 2023 was to **leverage scanning strategies that included dense vertical coverage to display how PAR can afford additional spatial coverage while maintaining rapid update volumes between 1.5 and 2 minutes**. Many of the scanning strategies also included revisits at the 0.5° elevation to maintain <1 minute low-level sampling. During 2023, the ATD operated exclusively in pencil beam mode (i.e., one transmit and one receive beam) while other transmission modes were under active development.

In addition, the ATD data collection prioritized examining the benefits of “range oversampling,” which helps to reduce the variance of the radar moments (Curtis and Torres 2011). Specifically, the ATD has a native range resolution of 37.5 m due to the use of pulse compression. However, six range gates are typically averaged to compute the final radar moments at 225 m gate spacing, reducing the variance of the data.

Finally, a central goal of the ATD data collection in 2023 was to begin building an archive of severe weather cases for use in the NOAA HWT. Although previous experiments have been undertaken in the HWT using SPY-1A data, dual-polarization PAR data has not yet been used in a HWT activity. Therefore, continuous datasets were prioritized as much as possible for use in the HWT to simulate what a NWS forecaster might use from one side of a four-faced PAR. HWT activities employing the use of ATD data began in Calendar Year (CY) 24 and will be the subject of a forthcoming NOAA/NSSL Technical Memo.

3. Data Collection Priorities in CY24

In 2023, the ATD was largely operated in a way that is typical of most current, conventional, rotating, parabolic weather radars with the use of plan position indicator (PPI)-based radar volumes heavily emphasized. However, PAR affords much more flexibility in scanning than conventional weather radar.

3.1 Scan Designs in CY24

Between CY23 and CY24, new capabilities were added to the ATD’s Human Machine Interface (HMI) that enabled the use of more creatively designed scanning than previously feasible. Some features include:

1. the ability to reposition the antenna while automatically pausing scanning in order to better position the ATD sector to maintain focus on a target or change targets;
2. the implementation of “Playlists” in scan design, which allows multiple scans (or antenna move commands) to be sequenced and repeated ; and
3. the addition of Linear Depolarization Ratio (LDR) mode (discussed in detail in Section 3.3).

As a result of the above features, the ATD’s main goal was to **achieve approximately one-minute volumetric updates while also leveraging the flexibility of the ATD to collect unique observations that are most practical with a PAR system.**

In contrast to CY23, cases that achieved ~one-minute *volume* updates were a central aim of the ATD. As in CY23, however, the ATD primarily operated in pencil beam mode. Therefore, in order to achieve a one-minute volumetric update, some elevation angles had to be strategically eliminated and/or reallocated. For example, Figure 3 shows the Supercell scanning strategy elevation angles targeted at supercells <50 km range from the ATD. In the 2024 strategy (Figure 3a), the mid-level coverage of elevation angles is reduced relative to the 2023 strategy (Figure 3b). However, reasonable coverage is maintained in the low levels to monitor hazards such as tornadoes and near-surface hail. Likewise in the upper levels, coverage is reallocated and slightly reduced, but reasonably maintained to monitor upper-level precursors to surface-level hazards such as hail growth. In CY25 (see Section 6.3), we will explore leveraging additional PAR-based scanning techniques to simultaneously reduce volume time and maintain optimal vertical coverage.

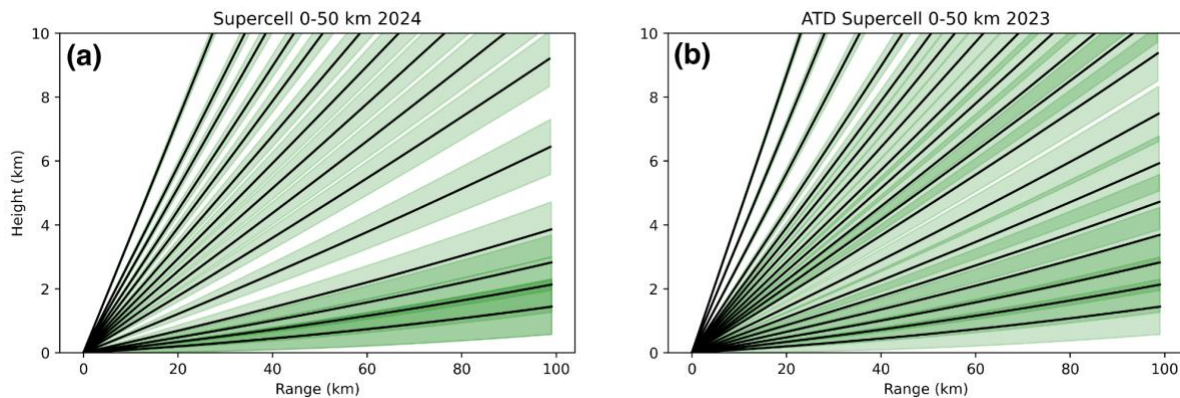


Figure 3. The elevation angles of the Supercell scanning strategy for supercells <50 km from the ATD for 2024 with 15 elevation angles (a) and 2023 with 19 elevation angles (b) are shown. In the figure, the elevation angle coverage in the low levels is very similar. In the mid-levels, the 2024 scanning strategy has reduced coverage in favor of redistributed coverage in the upper levels to monitor for upper-level precursor signatures such as hail growth.

In order to examine the benefits of PAR, the co-located NSSL WSR-88D (KOUN) was operated akin to an operational WSR-88D during CY24. KOUN was operated largely in Volume Coverage Pattern 212 (VCP212) with the Supplemental Adaptive Intra-Volume

Low Level Scan x2 (SAILSx2) technique enabled, which affords two *additional* 0.5° elevation cuts (three in total) per radar volume. KOUN acts as a comparison to PAR observations via the ATD within the ATD's 90° field of view², particularly in terms of temporal update and spatial coverage. However, we note that KOUN has a ~1° beamwidth compared to ATD's 1.6° beamwidth at broadside.

3.1.1 Traditional and Non-Traditional Scanning Strategies

“Traditional” radar volumes are collected using a sequence of horizontal scans (PPIs). By definition, each PPI is taken at a constant elevation angle with respect to the horizon, which is the most mechanically efficient method by which to collect data with conventional weather radars. A radar volume consists of a sequence of PPIs, which varies depending on the intent of the scanning strategy (e.g., a radar volume intended to target severe convection versus clear air return). In addition, the scan parameters such as the pulse length, pulse repetition time (PRT), and the number of samples per radar azimuth are varied depending on the intent of the scanning strategy. The combination of the total coverage (the number of beam positions in azimuth and the number of elevation angles desired), desired data quality (depends on the number of samples per beam position), and target volume time (depends on the PRT and the number of samples per beam position) must be balanced in order to optimize a scanning strategy. In CY23, the vast majority of the ATD scanning strategies were optimized to construct PPI-based radar volumes that included dense coverage in the vertical while maintaining rapid updates under 2 minutes (generally near 1.5 minutes). As already discussed, in CY24 the temporal update of the volume was prioritized.

However, most radars are not limited to PPI-based radar volumes. The WSR-88Ds can theoretically sample the atmosphere via range height indicators (RHIs), although they do not do so in operations. RHIs are not typically incorporated into operational radar scanning because of the strain on mechanical parts and the required time to change from PPI to RHI mode or capture multiple RHIs in sequence. However, capturing RHIs is simple with PAR due to the ability to near-instantaneously change beam positions. They are advantageous to characterize radar-observed kinematic and microphysical information nearly instantaneously in a vertical column. On the ATD in CY24, a key goal was to use the “Playlist” feature of the HMI to sequence traditional PPI volumes (again, of ~1 minute volumetric update time) followed by one or more RHIs through a target of interest. Note that any type of scan may be sequenced using the HMI Playlist feature

²Note that KOUN has a full 360° field of view. We again note that the ATD was built to demonstrate only one side of a four-faced panel PAR concept. A full-scale PAR system with four faces covering a full 360° field of view would have the same update time as the ATD with the four panels operating simultaneously. Comparisons of ATD and KOUN data, where appropriate, are made exclusively in the overlapping azimuthal sectors covered by both ATD and KOUN.

(e.g., PPIs, RHIs, a mixture of both, scans of different transmission modes). A typical single RHI takes approximately 1 second to complete. In CY24, RHIs were focused near and at broadside, as RHIs were only possible to define in antenna-relative coordinates. Capturing RHIs was made possible by an operator changing the antenna position to point the broadside direction of the antenna along the azimuth of the intended target (e.g., a tornadic mesocyclone). The ability to reposition the antenna with automated pausing and restarting of the scan sequence was key to making the collection of RHIs most efficient. Future designs of RHI sequencing are expected to allow an earth-relative azimuth to be input to the RHI(s) “on the fly” to increase efficiency and limit antenna movement.

3.1.2 Linear Depolarization Ratio

In addition to RHI sequencing, another non-traditional scan mode was incorporated at times between or within “traditional” PPI-based radar volumes: LDR scans (PPI or RHI based). LDR is unknown to many, as it is not collected by the WSR-88Ds in addition to most research radars and has not been studied in-depth since the early days of weather radar research. As such, we briefly review it here.

LDR mode includes transmitting in the horizontal polarization only and receiving in both the horizontal and vertical directions. The variable, LDR, is then the ratio of the backscattered power in the cross-polarization (vertical) direction to the backscattered power in the co-polar (horizontal) direction. LDR is shown in Eq. (1),

$$LDR = 10 \log_{10} \left(\frac{Z_{vh}}{Z_{hh}} \right) (1),$$

where the left subscript represents the polarization of the received backscatter (horizontal h or vertical v) and the second subscript represents the polarization of the transmitted wave. The radar reflectivity Z is shown in units of $\text{mm}^6 \text{m}^{-3}$. We note for the reader that LDR is almost always negative in its logarithmic form, as the scattering in the cross-polarization direction is typically far less than the scattering in the co-polar direction. LDR is sensitive to the canting angle of particles as well as their shapes and dielectric constants (Melnikov et al. 2019; Kumjian et al. 2020). For raindrops, LDR is typically < -25 dB. It can be enhanced in the melting layer (i.e., near -20 dB) and in refreezing layers (Kumjian et al. 2020) and also begins increasing nearly monotonically with hail size (Mirkovic et al. 2022).

Most radars employ simultaneous transmit and receive (STR) mode to capture dual-polarization moments. The cross-polarization backscatter is, therefore, masked by the comparatively strong co-polar return in STR mode. Time is added for a scanning strategy if both STR (to collect dual-polarization moments) and LDR modes are employed. Alternating transmission and simultaneous receive (ATSR) mode can be employed to capture the full dual-polarization matrix, but again at the expense of time.

With PAR, electronic scanning affords flexibility to capture such modes, however, while minimizing time expended to do so. In CY24, LDR PPIs and/or RHIs were incorporated into scanning strategies by collecting, for example, a single 0.5° elevation LDR PPI or LDR-based RHIs as described for dual-polarization RHIs in Section 3.1.

3.1.3 A Brief Review of Engineering Scan Designs

As briefly outlined in the CY23 report (Alford et al. 2024), self-consistency scans were used periodically to evaluate the accuracy of ATD's dual-polarization calibration products obtained with the calibration tower. The biases in dual-polarization measurements are a function of beam steering direction and necessitate precise correction at each beam position. The correction factors for reflectivity, differential reflectivity, and differential phase are derived by accurately characterizing copolar pattern main beams at relevant beamsteering angles. To independently assess the calibration accuracy, a self-consistency test utilizes data from a sequence of sector scans conducted with the antenna at progressively different mechanical positions. By processing data from overlapping sectors between adjacent scans, radar variables for the same hydrometeors are derived at varying electronic beamsteering angles. Consistency in the data across consecutive scans thus verifies the effectiveness of beamsteering dual-polarization calibration. In particular, the initial self-consistency scans are performed by collecting a rapid-update radar volume, usually consisting of multiple elevation angles. The physical position of the ATD antenna is changed by $\pm 10^\circ$, $\pm 20^\circ$, or $\pm 30^\circ$ azimuth and radar volumes are collected in succession so that the sector scans overlap. By assuming the dual-polarization measurements from the multiple radar volumes are approximately the same, the beam steering corrections applied to the estimates of reflectivity and dual-polarization variables can be evaluated. Thus far, the self-consistency scans collected suggest that the ATD's dual-polarization beamsteering bias correction factors are accurate (Ivić et al. 2023), implying that data from the ATD are useful for achieving R&D goals under the NSSL PAR Program.

Further reductions in volume update time may be achieved by employing PAR-specific beamforming concepts. One promising approach is the use of "spoiled transmit beams". In this approach, the transmit beams are deliberately widened to illuminate a larger area and multiple receive beams are formed simultaneously. This achieves instant broader coverage with some (known) tradeoffs in sensitivity and angular resolution (cf., Ivić 2024, Ivić 2025), resulting in faster volume update times. Initial calibration of spoiled beams using the ATD calibration has occurred and further refinement is ongoing. We are also exploring the use of weather data to derive the spoiled beam calibration products. For this purpose, we designed scanning strategies that alternate pencil and spoiled beam transmissions to collect radar data that could be used to estimate differences between radar variables obtained using pencil and spoiled beams. Because the corrections for pencil beams were available, the corrections for spoiled beams were computed by

combining the pencil beam corrections and the differences estimated using collected data.

3.2 Observing Objectives

In addition to the scan design objectives reviewed above, four categories of research were emphasized in CY24 given the capabilities of the ATD at the time. Four objectives were prioritized in data collection with which to accelerate the NSSL PAR Program's Research and Development.

3.2.1 On the Operational Benefits of PAR

The first objective of CY24 was to ***collect a wide variety of cases that may be used for operational demonstration, including those employed in the NOAA HWT PAR activities***. PAR may be able to provide additional information to forecasters in a potential future operational setting by better resolving severe weather signatures (e.g., tornado vortex, tornado debris, dual-polarization) and general radar signatures (e.g., rapid changes in hydrometeor type, precipitation intensity) in four dimensions. As such, capturing operational-like datasets with which PAR may be evaluated in formal (e.g., the NOAA HWT) and informal (i.e., public conferences and meetings, reports, one-on-one discussions) settings is a leading priority of the NSSL PAR Program.

3.2.2 Fundamentals of Severe Weather Research

A second objective of CY24 was to ***collect detailed observations of severe weather signatures, particularly dual-polarization signatures, with which kinematic and microphysical processes may be better understood***. For example, fundamental topics being addressed in the severe weather community include tornadogenesis processes, quasi-linear convective system (QLCS) mesovortex processes, severe hail growth, lightning, heavy rainfall, and the relationships between microphysics throughout storms and their subsequent impacts on storm kinematics and near-surface hazards. Each of the aforementioned topics represent very rapidly evolving processes that are often poorly resolved in both space and time by conventional weather radars. Hence, PAR may enable more comprehensive understanding of severe weather processes through the collection of a wide variety of severe weather cases in central Oklahoma.

3.2.3 Radar Polarimetry

As mentioned in Section 2.1, a critical question of PAR is its ability to integrate dual-polarization measurements. Now that it is known that dual-polarization PAR observations are achievable, there exists a wealth of potential observations that may drive

the understanding of polarimetry forward. As such, the third objective of CY24 was to ***capture novel dual-polarization data with the ATD PAR for a deeper understanding of precipitation microphysics***. LDR data and rapid-update dual-polarization data may provide insight into hydrometeor classification, hydrometeor sizing, mapping mixed precipitation, and quantifying hydrometeor statistics (e.g., canting angles). Ultimately, improving the understanding of precipitation microphysics via observations may lead to improvements in numerical weather prediction parameterizations as well as observationally-derived precipitation products.

3.2.4 Engineering Demonstration

To implement advanced techniques on the ATD, collaboration between the engineering and meteorological teams at NSSL is often required. Engineers at NSSL routinely collect data for ATD calibration purposes (as one example) separate from or in conjunction with meteorological data collection. However, hybrid collections (i.e., combined meteorological and engineering collections), where testing new modes and scanning techniques are benefitted by weather data, were also incorporated into the data collection goals in CY24. Hence, the fourth objective in CY24 was to ***incorporate engineering testing into weather collection when weather observations can lead to the improvement and/or validation of PAR-based scanning techniques and modes***. Such techniques can include adaptive scanning, which is discussed above in Section 2.1.

4. CY24 Dataset Overview

As in CY23, a wide variety of weather events were sampled by the ATD including tornadic supercells, non-tornadic and tornadic QLCSs, downbursts, mesoscale convective systems (MCSs), hail producing supercell and multicell storms, winter weather events, and fire weather smoke plumes. At least 145 hours of meteorologically relevant data were collected across 45 separate events throughout CY24³. The cases were loosely categorized into the following categories according to their predominant storm mode/hazard as follows: supercells, severe/non-severe MCSs, severe multicell convection, non-severe multicell convection, downbursts, winter weather, and clear air and engineering tests (includes fire weather). The number of cases in each category is listed in Table 1.

³ Note that the number of hours of data collected only represent data deemed meteorologically relevant and do not include a wealth of non-meteorological data collected for calibration, signal processing development, and other engineering and testing purposes.

Tornadoic Supercells	Severe and Non-severe MCSs	Severe Multicell Convection	Nonsevere Multicell Convection	Downbursts	Winter Weather	Clear Air and Engineering Tests
7	10	10	3	1	3	11

Table 1. Storm-type event counts collected by the ATD in CY24. The total number of cases summed across all categories is 45.

A list of all cases collected by the ATD is given in Appendix 1. Details regarding the times observed, the scanning strategy(s) used, and the sector(s) used are given.

5. Demonstrating the Benefits of PAR in CY24

After another successful year of data collection with the ATD, additional insight is provided into the potential operational and research benefits that PAR technology can provide. Relative to the CY23 Data Collection Report (Alford et al. 2024) where summaries of individual cases were highlighted to bring attention to the wide variety of observations captured in CY23, we instead focus here on highlighting the insights gained *about PAR* and use a subset of cases as demonstrations. Again, a full list of cases may be found in Appendix 1, which emphasizes the wide variety of cases sampled by the ATD in CY24.

5.1 Potential Operational Benefits

A key question relevant to the NWS AoA for the next generation of weather radar in the United States is how PAR may be beneficial to operations. We first focus on the rapid updates afforded by PAR in terms of low-level sampling and then in terms of volumetric resolution. Note that many of the other concepts explored in the following sections (5.2-5.4) are also highly relevant to future operational benefits, although they are more strongly discussed from a research and development perspective.

5.1.1 Rapid-Update Low-Level Data

A well known benefit of PAR is the ability to collect rapid update data to monitor, for example, severe hazards such as tornadoes. Datasets collected by the ATD since 2023 are no exception and continue to demonstrate such a benefit. Currently, the WSR-88Ds can leverage the SAILS technique to decrease the time between revisits at the 0.5° elevation. The SAILSx3 allows for a best possible 90 seconds between 0.5° elevation scans. However, it is known that many tornadoes last <90 seconds or can rapidly spin up between 90-second scans. Critical messaging can be impeded by the delayed radar-

based detection of tornadoes that form and dissipate between radar scans or evolve rapidly between radar scans. Post-event estimation of tornado formation time/location, dissipation time/location, and track can likewise be benefitted by an increase in temporal resolution of 0.5° elevation scans.

The ATD scanning strategies in CY24 targeted at tornadoes often included SAILS-like updates wherein the 0.5° elevation was revisited every 30-45 seconds, depending on the exact specifications of the scanning strategy being performed. On 27 April, a series of tornadoes was produced by an embedded supercell-like structure on the northern portion of a convective line. One of the tornadoes formed to the southwest of the ATD, which produced a tornado debris signature (TDS), observed by the ATD and KOUN. In Figure 4, a PPI sequence of the TDS in correlation coefficient (ρ_{HV}) is shown. At 0153:14 UTC, no TDS was observed by KOUN or by the ATD. The first image shown in Figure 4 from the ATD is about one minute later at 0154:09 UTC, where there is a weak reduction in ρ_{HV} . However, about 40 seconds later 0154:53 UTC, the TDS is clearly observed by the ATD. At 0155:06 UTC, KOUN likewise observes the TDS. In the subsequent times, the TDS persists in both radar datasets.

Focusing on the ATD data specifically, it is difficult to confirm a TDS at 0154:09 UTC, as the signature is rather weak. However, it is not only the first appearance of a TDS that is important, but also the persistence and trend of the TDS in time. With the SAILSx2 strategy employed by KOUN, 0.5° elevation updates were approximately every 2-3 minutes. In NWS operations, SAILSx3 may be employed to reduce the update to ~90 seconds. However, even in the span of a 90-second window, three 0.5° elevation updates are achieved by the ATD, providing the opportunity to assess the trends and persistence of signatures such as a weak and/or developing TDS in a sub-90-second window.

ATD

KOUN

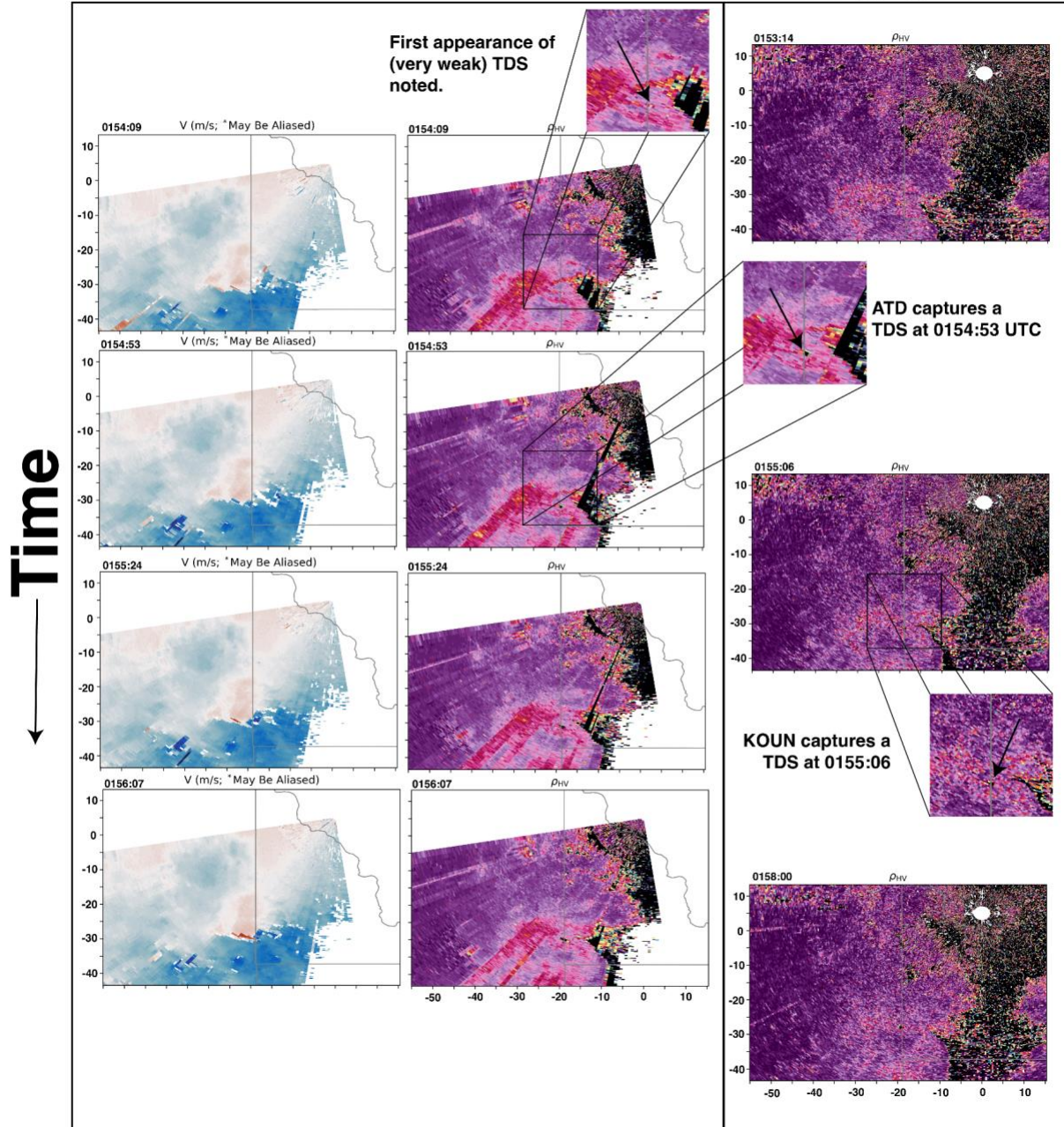


Figure 4. A time series (time increases toward the bottom of the figure) of Doppler velocity (shown for context) and correlation coefficient from ATD (left) and KOUN (right) on 28 April 2024. The subpanels each show ρ_{HV} as a function of time at the 0.5° elevation. In the ATD data, a TDS appears at 0154:09 UTC. The same TDS does not appear until 0155:06 UTC in KOUN data. Note that there are some regions of errors associated with an experimental dealiasing scheme in the ATD Doppler velocity plots.

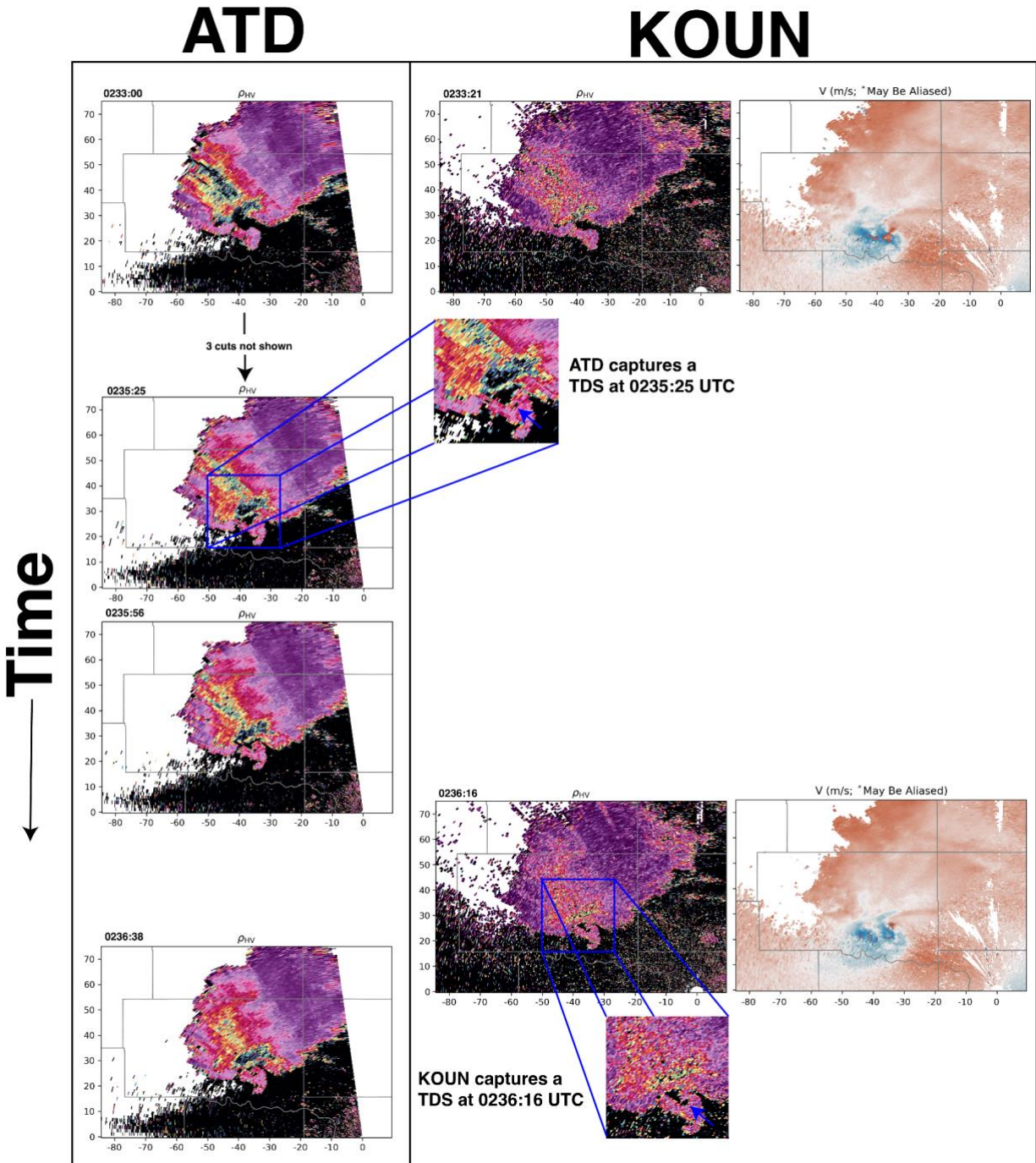


Figure 5. A time series (time increases toward the bottom of the figure) of correlation coefficient from ATD (left) and correlation coefficient and Doppler velocity from KOUN (right) on 20 May 2024. The subpanels each show ρ_{HV} as a function of time at the 0.5° elevation. In the ATD data, a TDS appears at 0235:25 UTC. The same TDS does not appear until 0236:16 UTC in KOUN data. The aliased Doppler velocity data from KOUN are shown for context.

Another similar case wherein a TDS was observed by the ATD between KOUN scans was captured on 19-20 May 2024. In Figure 5, a tornadic supercell is shown as it entered

the Oklahoma City metropolitan area from west to east. An EF-2 tornado was confirmed by the NWS that began near 0228 UTC. At about 0233 UTC, both the ATD and KOUN observed the tornadic supercell, but did not observe a TDS at the 0.5° elevation. The ATD collected three additional 0.5° elevation cuts (not shown) until a TDS formed near 0235:25 UTC. About one minute later, the next 0.5° elevation cut was collected by KOUN at 0236:16 UTC at which point a TDS can be seen in the ρ_{HV} data.

TDS signatures such as those in Figures 4 and 5 often serve not only as a confirmation for a warning, but also as a way to tailor messaging to the public through updates to the warning information. Detecting TDS signatures at the 0.5° elevation is but one example of the benefits of rapid update, low-level data via a PAR system. In addition, rapid-update PAR data can provide insight into the consistency of signatures in time, providing additional confidence that an observed signature such as a weak TDS (e.g., Figure 4) is not a radar artifact or associated with, for example, large hail or biological scatterers. The operational benefits of PAR data, including how rapid-update data may impact warning decisions and confidence, is being tested in the NOAA Hazardous Weather Testbed and will be expanded upon in Kuster et al. (2025, in preparation).

5.1.2 Volumetric Updates

As discussed in the previous subsection, rapid update data at the 0.5° elevation can be beneficial to monitor low-level severe hazards such as TDSs. The earlier detection and temporal consistency in a rapid-update framework may provide additional confidence to a forecaster in an operational setting. However, typical radar volumes include many additional elevation angles above 0.5° with which the vertical continuity of signatures such as TDSs may be evaluated. Likewise, precursor signatures in the mid- and upper-levels may also provide insight into severe weather later experienced at the surface.

As previously discussed in section 5.1.1, multiple tornadoes were observed during the 27-28 April event. Early during operations near 2100 UTC, a tornadic supercell was observed ~100 km west of the ATD. The ATD employed the use of a long-range scanning strategy that focused elevations at and below 10° that updated in just over one minute. Near 2110 UTC, a tornado was confirmed by the NWS near Hinton, OK. In Figure 6, volumetric renderings of so-called “normalized rotation⁴” are shown. The ATD and the nearby KTLX radar (the Oklahoma City area WSR-88D) observed a relatively disorganized low-level mesocyclone near the beginning of each radar’s ~2107 UTC radar volume. The ATD collected its next radar volume near 2109 UTC. An intensifying and vertically coherent low-level mesocyclone on the southwest portion of the storm can be seen in the figure. At 2110 UTC, the low-level mesocyclone had deepened and intensified

⁴ Normalized rotation is a derived product from the Gibson Ridge (GR) 2 Analyst software package. The product is derived from Doppler velocity.

further, coincident with tornadogenesis. The trend in low-level mesocyclone intensification, deepening, and organization continued through 2112 UTC.

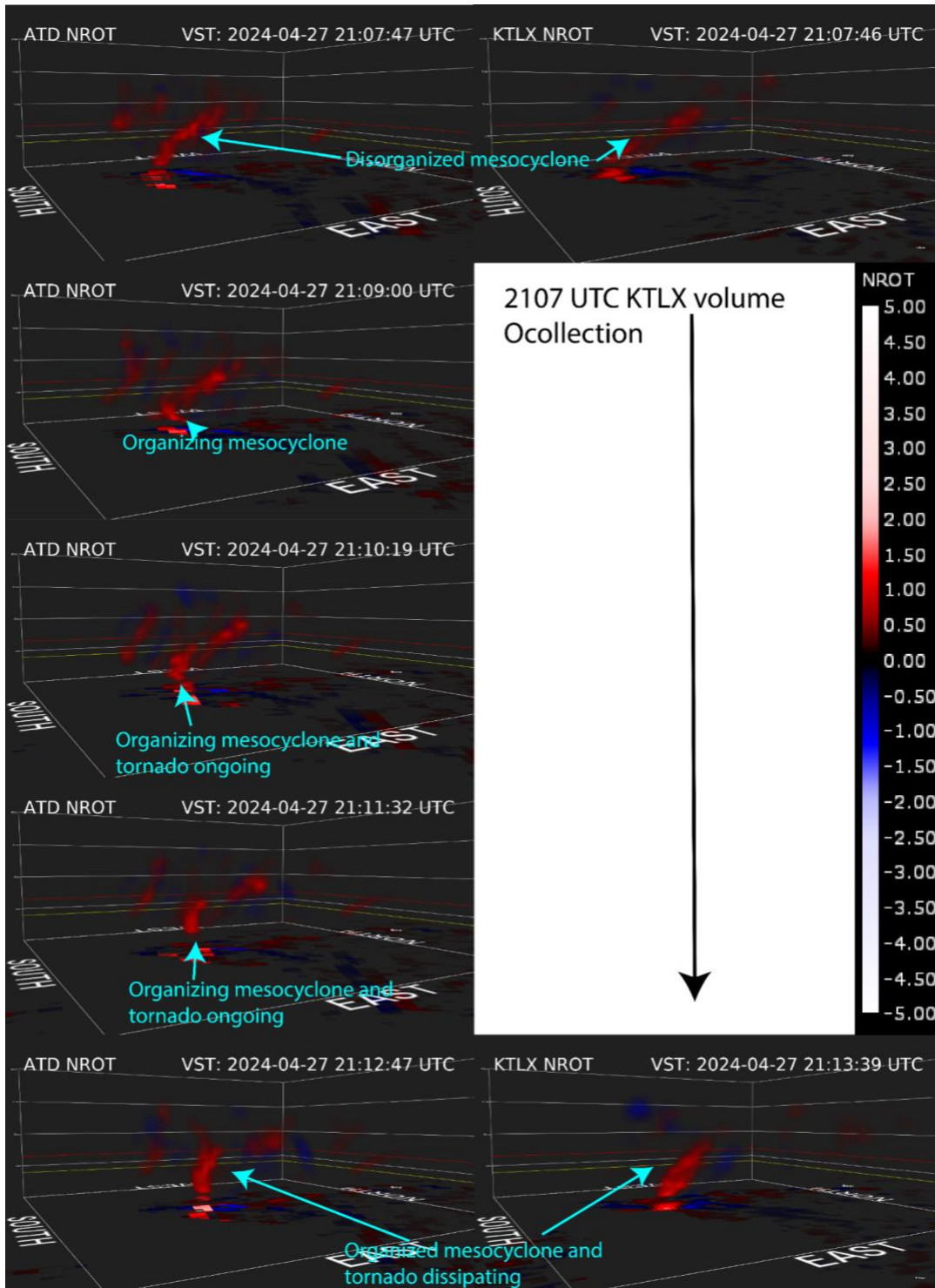


Figure 6. A time series (time increases toward bottom) of three-dimensional isosurfaces of “normalized rotation” computed in GR2Analyst. On the left, ATD volumes of normalized rotation are shown (red is cyclonic). On the right, KTLX volumes are shown. In the figure, the mesocyclone (indicated by the red isosurfaces) are disorganized in the initial ATD and KTLX volumes near 2107 UTC. The ATD, using just over 1-minute volume updates, captured the volumetric evolution, organization, and intensification of the mesocyclone prior to a confirmed tornado occurring at 2110 UTC. KTLX, on the other hand, required about 6 minutes to capture a full volume. “VST” in the figure refers to the radar “volume start time.”

The structure of the mesocyclone is generally better resolved by the ATD. In the KTLX data, there is a significant tilt in the mesocyclone from west to east associated with the propagation of the storm over the ~6-minute volume time. The best comparison in the figure is near 2113 UTC for the ATD and KTLX where the mesocyclone is more upright in the ATD volume at 2112:47 UTC versus heavily tilted in the 2113:39 UTC KTLX volume. Such artificial tilt not only biases the structure of kinematic data, but also other signatures as well such as differential reflectivity (Z_{DR}) columns which are related to the updraft structure.

At 2113 UTC, KTLX began its next volume with the 2107 UTC volume spanning ~five full ATD radar volumes. The 2113 UTC KOUN volume, which began after the tornado had dissipated at 2112 UTC (according to the NWS), shows a better organized mesocyclone in Figure 6 than the previous 2107 UTC volume. In the time required to capture the 2107 UTC KTLX volume, the ATD observed the consolidation, organization, and intensification of the low-level rotation using rapid-update radar volumes. Similar to that of the rapid low-level updates discussed in section 5.1.1, the trends in mesocyclone structure and intensity are much better resolved by the ATD PAR.

Volumetric updates are not only important for assessing low-level hazards, but also for evaluating precursor signatures. So-called specific differential phase (K_{DP}) cores (Kuster et al. 2021) are defined as intense localized maxima in K_{DP} . They typically are associated with regions of melting hail and/or high concentrations of raindrops. In downburst-producing storms, Kuster et al. (2021) showed that the development of K_{DP} cores near the environmental freezing level always preceded downburst development near the surface. Stronger K_{DP} cores also tended to be associated with stronger downbursts. The study employed the use of WSR-88D data to show that the near 5-minute volume scans of the WSR-88Ds were typically sufficient to observe the *existence and general evolution* of K_{DP} cores, but faster volume updates were more likely to sample the true *magnitude* of the K_{DP} cores.

Figure 7. A time series (time increases toward the bottom of the figure) of K_{DP} from ATD (left) and KTLX (right) on 15 August 2024. The subpanels each show K_{DP} as a function of time at the 3.7° and 3.1° elevation surfaces from the ATD and KTLX, respectively. In the ATD data, two periods of intensification of the K_{DP} cores are observed. In the KTLX data, the periods of intensification are not resolved.

On 15 August, the ATD and KTLX observed a downburst-producing thunderstorm that resulted in 60 and 71 mph wind gusts near Minco, OK at 2330 and 2335 UTC, respectively. Using the 3.7° and 3.1° PPIs from ATD and KTLX, respectively, Figure 7 shows a time series of the near-freezing level K_{DP} . In the ATD time series, two periods of intensification of K_{DP} cores were observed. The first intensification period began ~9 minutes prior to the 2330 UTC 60 mph report at the surface. The second period of intensification began ~9 minutes prior to the 2335 UTC 71 mph report at the surface. Although more thoroughly linking both reports with the individual K_{DP} core surges requires additional analysis, the time of the K_{DP} core intensification to severe winds at the surface is consistent with Kuster et al. (2021). In addition, ongoing research suggests that strong K_{DP} cores on the order of 4° km^{-1} (as in Figure 7) preceded surface downburst development by about 5 minutes on average. As such, it is plausible the bursts of severe winds in this case are associated with rapid fluctuations in the K_{DP} core evolution.

In the KTLX data, the temporal update rate of the radar volume was insufficient to observe the K_{DP} core evolution. As shown in Figure 7, the earlier observation time showed an intense K_{DP} core that is consistent with K_{DP} cores capable of producing a downburst. However, the next observation at the same elevation from KTLX showed a weakening trend in K_{DP} . Similar to the results of Kuster et al. (2021), the intra-volume temporal evolution of the K_{DP} core is not resolved by the slower update rate, entirely missing the two intensification periods observed by the ATD.

5.2.3 Introducing Flexible, Non-Traditional Scanning

Currently with the operational WSR-88Ds, RHI scanning is not performed. RHIs, when captured, provide excellent vertical coverage and a nearly instantaneous sense of microphysical and kinematic processes ongoing in a vertical column. Artificial tilt in storms can make diagnosing the vertical alignment supercells, for example, difficult, which has been shown to be helpful in distinguishing between tornadic and non-tornadic thunderstorms (Homeyer et al. 2020). In operational settings, the only possible way to leverage an RHI framework is to take advantage of pseudo-RHIs that are reconstructed from full WSR-88D volume scans. An example of such is shown in a small MCS observed by KOUN on 7 May 2024 in Figure 8. The pseudo-RHI is taken at 280° azimuth on the northern portion of a near-surface bowing segment. The elevation angles that comprise the pseudo-RHI are taken at significantly different times, resulting in an artificial tilt of all signatures due to storm motion. Most notably, the reflectivity features such as the

reflectivity maximum near 25 km range and 6-8 km altitude are unclear with respect to the vertical alignment relative to the core at 28 km range below 4 km altitude. In the Doppler velocity data, it is generally unclear if the strong (aliased) velocities may be penetrating to the near-surface due to the significant time between the lowest elevation angle and the rest of the elevation angles above. In the Z_{DR} data, the top of the melting layer is difficult to distinguish as is the presence of a potential Z_{DR} column near 21 km in range.

As mentioned in section 3.1.1, the ATD captured routine RHIs between more traditional volume scans. In general, each RHI took on the order of 1 second to complete, providing a nearly instantaneous measurement of all data in the vertical. Figure 9 shows an example, which was taken approximately half way through the volume scan that yielded the pseudo-RHI in Figure 8. It can be seen that the artificial tilt induced in the pseudo-RHI from KOUN (Figure 8) is eliminated in the true RHI from the ATD (Figure 9). Additional details that were unclear in the pseudo-RHI from KOUN are much clearer in the true RHI from ATD. Regions of high reflectivity at 25 km range above 6 km can be seen and are likely associated with growing hail and graupel in the updraft of the MCS. In the velocity field, the region of most-intense (aliased) Doppler velocities can be seen to extend to the lowest sampled elevation angle, suggesting that the potential severe winds are near or just above the surface. In addition, an intense “rotor” feature can be seen atop the cold pool structure. In the Z_{DR} field, a Z_{DR} column is apparent at the front of the cold pool and is below the region of growing hail/graupel identified in reflectivity.

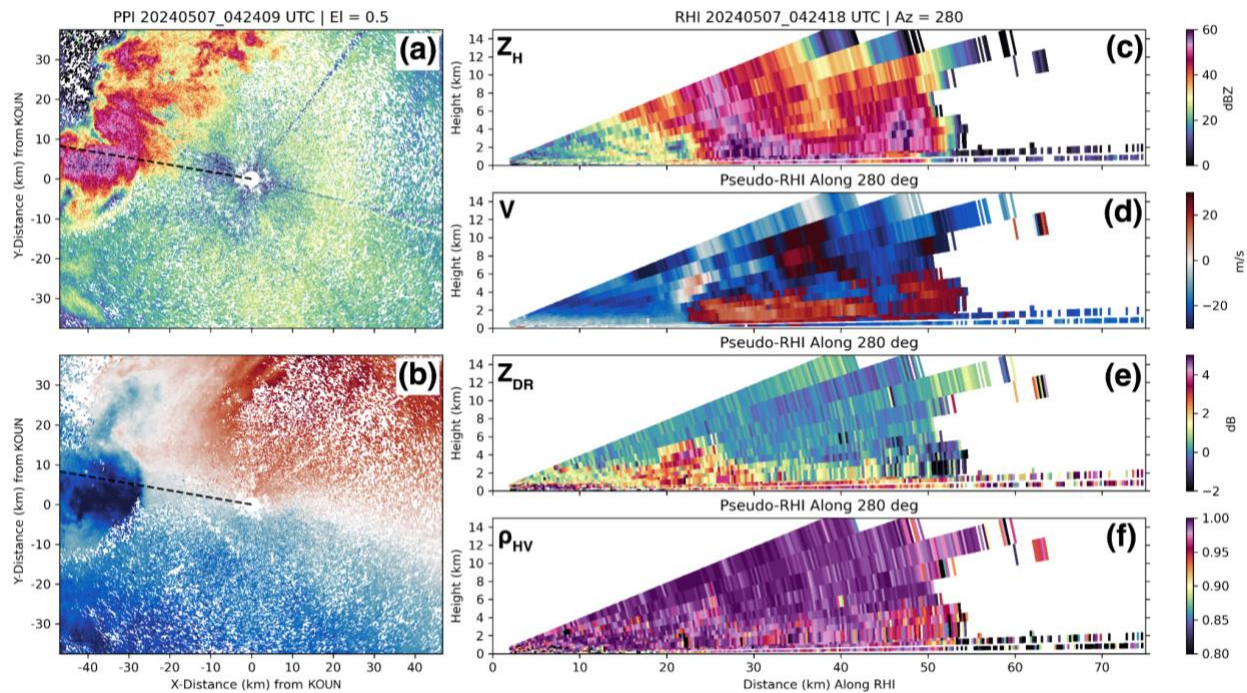


Figure 8. A pseudo-RHI at 280° azimuth is shown reconstructed from the 0424:09 UTC volume scan from KOUN. In the left column (panels a and b), PPIs of (a) radar reflectivity and (b) Doppler velocity show a small MCS to the west of KOUN. The dashed black line shows the location of the pseudo-RHI, which is taken through a region of high reflectivity and on the northern side of a region of intense inbound Doppler velocities associated with a small bowing segment. In the right column, the pseudo-RHI (c) reflectivity (also indicated as Z_H), (d) Doppler velocity (also indicated as V), (e) Z_{DR} , and (f) ρ_{HV} are shown from top to bottom.

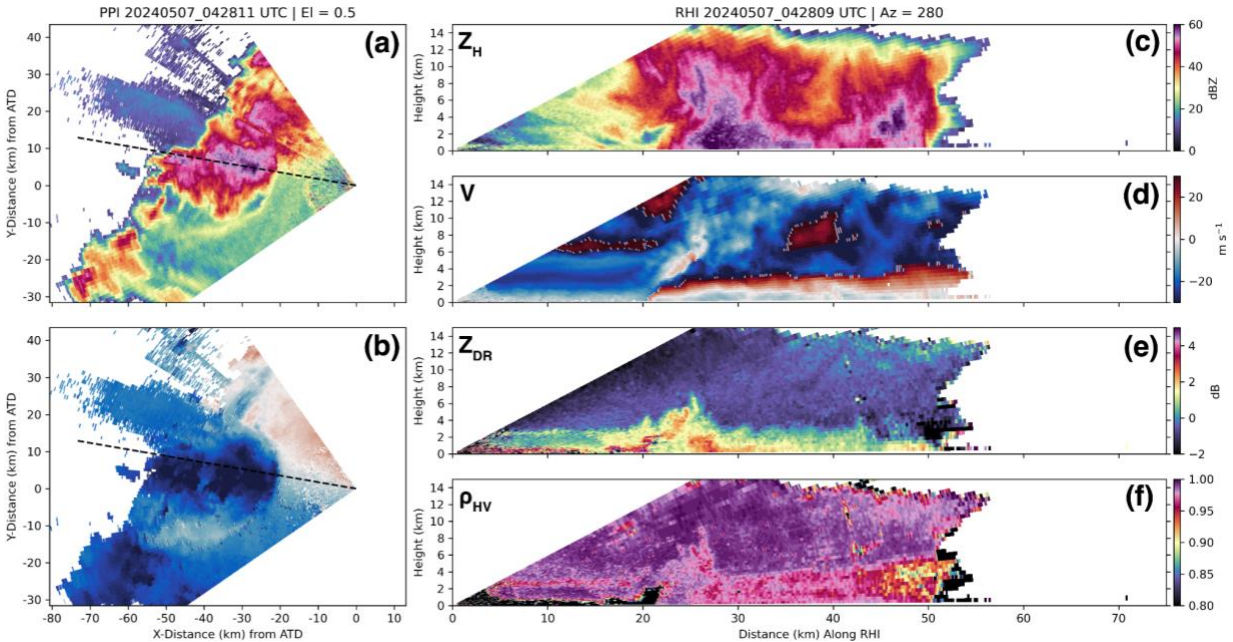


Figure 9. A true RHI at 280° azimuth is shown taken at 0428:11 UTC by the ATD. In the left column (panels a and b), PPIs of (a) radar reflectivity and (b) aliased Doppler velocity show a small MCS to the west of the ATD. The dashed black line shows the location of the pseudo-RHI, which is taken through a region of high reflectivity and on the northern side of a region of intense inbound Doppler velocities associated with a small bowing segment. In the right column, the true RHI (c) reflectivity (also indicated as Z_H), (d) Doppler velocity (also indicated as V), (e) Z_{DR} , and (f) ρ_{HV} are shown from top to bottom.

5.2 Severe Weather Observations

As a part of the NSSL PAR Program, the data collection objectives with the ATD encompass capturing observations of rapidly evolving severe weather with which to advance the fundamental understanding thereof. In CY24, a wide array of datasets were captured to focus on tornadoes, severe winds, hail, and flooding, similar to the breadth of cases captured in CY23 (Alford et al. 2024).

5.2.1 A Non-Tornadic Mesovortex

A critical area of interest in the severe weather research community is investigating the microphysics, kinematics, and radar signatures of severe winds and tornadoes produced by QLCS mesovortices (e.g., Ashley et al. 2019; Kuster et al. 2024). In CY23, Alford et al. (2024) noted the plethora of tornadic mesovortices produced by the 27 February 2023 QLCS in central Oklahoma. Most (if not all) of the mesovortices observed during that case were tornadic, leaving few opportunities for comparison between non-tornadic and tornadic mesovortices. During 2 May 2024, however, an MCS/QLCS produced several non-tornadic mesovortices near Chickasha, OK. A particularly prominent mesovortex did produce a 69 mph wind measurement in Acme, OK at 0600 UTC. Figure 10 shows the initial evolution of the region of severe winds beginning about ten minutes prior to the severe wind report at Acme. Initially, the mesovortex observed by the ATD at 0550:22 UTC shows a relatively compact mesovortex structure embedded in a region of moderate ($2\text{-}3^\circ \text{ km}^{-1}$) K_{DP} . Some resemblance of a so-called “ K_{DP} drop” (cf., Kuster et al. 2024) can be seen, such that a minimum in K_{DP} behind the main convective line intrudes toward the front of the convective line. On the next scan from the ATD at 0550:54, the K_{DP} drop becomes more readily apparent, as does a local maximum within the convective line at the leading edge of the K_{DP} drop region. Just over a minute later at 0552:02 UTC, the region of highest Doppler velocities has greatly expanded. The expansion of the area of strongest radar-observed winds is coincident with the appearance of a strong K_{DP} maximum within the convective line ($>4^\circ \text{ km}^{-1}$) and the continued expansion of the K_{DP} drop behind the convective line. This evolution largely resembles the evolution of tornadic mesovortices in Kuster et al. (2024) with the critical exception that the mesovortex itself broadens, rather than consolidates. Although it is possible that a tornado was produced and not observed, the evolution of the Doppler velocities does indeed suggest a relatively broad region of severe winds, rather than the consolidation into a mesovortex capable of producing a tornado.

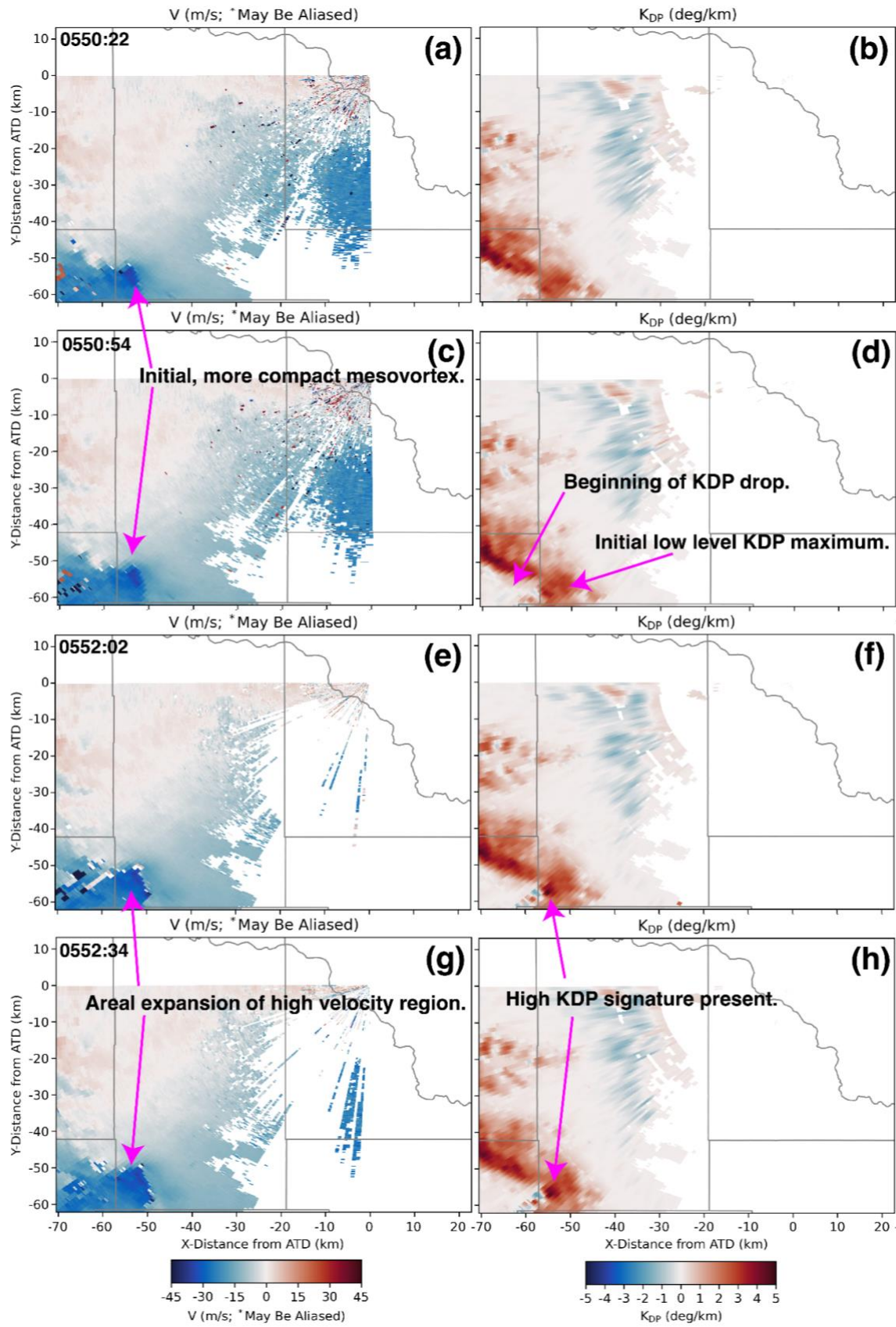


Figure 10. The evolution of a non-tornadic mesovortex from 2 May 0550:22 to 0552:34 UTC is shown. In panels (a), (c), (e), and (g), Doppler velocity is shown. In panels (b), (d), (f), and (h), K_{DP} is shown. Initially at 0550:22 UTC (a and b), the mesovortex in the figure is relatively compact. The K_{DP} drop behind the main convective line and low-level maximum in K_{DP} within the convective line begins primarily in the next time step at 0550:54 UTC (c and d). The mesovortex subsequently broadens in area coinciding with the enhancement of the K_{DP} drop behind the convective line and intensification of the local K_{DP} maximum in the convective line at 0552:02 UTC (e and f) and 0552:34 UTC (g and h). The data are shown at 0.5° elevation.

At 0557:33 UTC just before the report at Acme, the radar presentation of the mesovortex reached maturity. In Figure 11, the region of strong Doppler velocities had continued to expand in area. Several local maxima in the Doppler velocity field can also be seen, which appear to likewise be associated with local maxima in K_{DP} . Additional variability in the spectrum width (SW) and Z_{DR} fields can be seen, but are not discussed further here. Although we have focused on the 0.5° evolution of the mesovortex for brevity, additional insight into the full four-dimensional evolution of the pre-severe winds from a kinematic (Doppler velocity) and microphysical (dual-polarization data) will be a focus with this case to document the similarities and differences between tornadic and non-tornadic mesovortices.

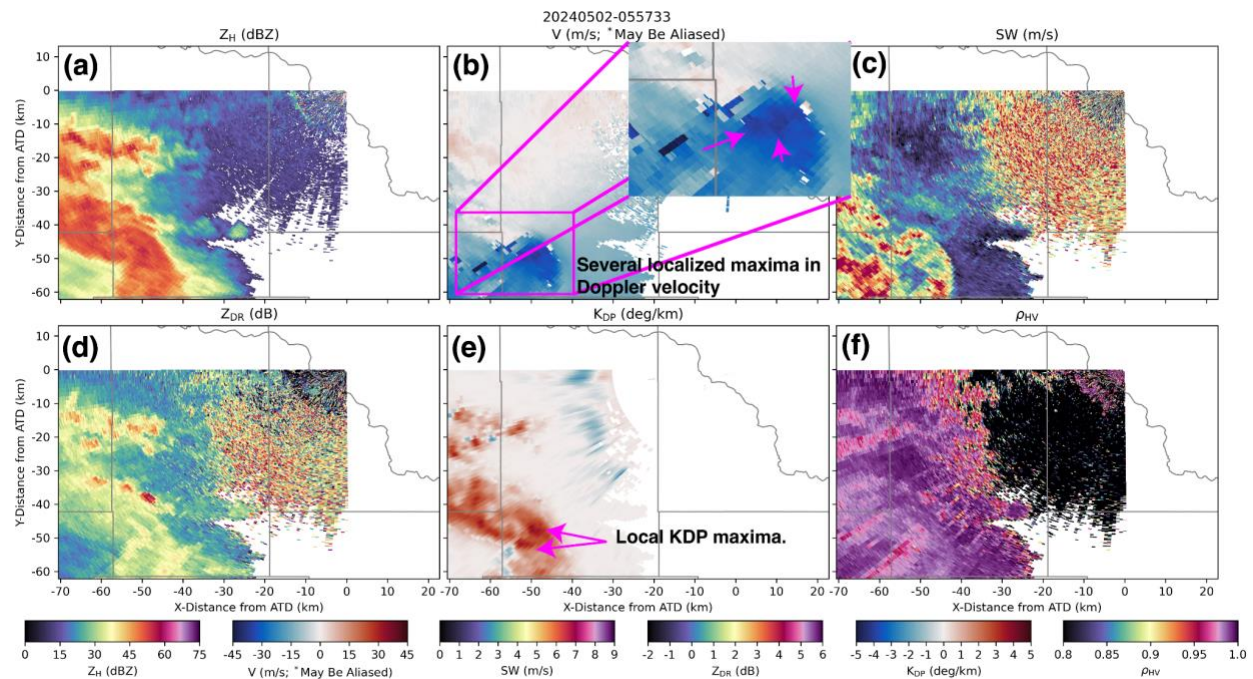


Figure 11. Dual-polarization data from the 2 May 0557:33 UTC PPI is shown, highlighting the mature presentation of a non-tornadic mesovortex. From top left to bottom right, panels of (a) radar reflectivity, (b) Doppler velocity), (c) SW, (d) Z_{DR} , (e) K_{DP} , and (f) ρ_{HV} are shown. The inset in (b) zooms in on the localized maxima in Doppler velocity within the broader mesovortex structure. Several maxima in the K_{DP} field are also indicated to bring attention to the near-co-location and possible relationship between the Doppler velocity and K_{DP} maxima.

5.2.2 Toward Precipitation Estimation

A relatively unexplored topic in PAR research is how well-calibrated PAR systems perform in terms of quantitative precipitation estimation (QPE) and if there are benefits (or lack thereof) to QPE from rapid updates and/or PAR-specific beamforming techniques (e.g., beam spoiling). The wide array of cases collected by the ATD in CY24 affords the opportunity to test current QPE algorithms to determine what improvements (if any) may be yielded by PAR observations.

A Ph.D. student project is currently aiming to examine how the ATD's rapid update data may benefit QPE by comparing QPE retrievals from the ATD and KOUN in a single-radar framework. To do so, multiple cases with a mixture of convective modes (i.e., supercells, MCSs, multicell convection, etc.) were combined to quantify the performance of QPE retrievals between the ATD and KOUN. The cases include 27 April (supercells, MCS; Figures 4 and 6), 30 April (supercells; figure not shown), 2 May (MCS/QLCS; Figures 10-11), 6 May (supercells, multicell convection; Figures 8-9), and 19 May (supercells; Figure 5). Each of these cases present rapidly-evolving scenarios where rapid scan observations may particularly benefit QPE retrievals. Again, KOUN was operated in SAILSx2 mode for these cases.

In Figure 12, KOUN and ATD QPE retrievals are compared in 5-minute increments to observed rain gauge data (primarily from the Oklahoma Mesonet). In the composite observations spanning the five contributing cases, it can be seen that the QPE retrievals with the ATD perform statistically better (KOUN has a root mean square error [RMSE] of 0.053 inches and ATD has a RMSE of 0.0376 inches). Visually and according to the permutation test for the Pearson Correlation, there is also significantly less scatter in the distribution such that the ATD QPE retrievals are much closer to the one-to-one line than the comparative KOUN data. KOUN also tends to have an underestimation bias for rain rates above 0.1 inches that is not seen in ATD data. A manuscript (Blumenauer et al. 2025, in preparation) is being drafted and will provide full details about the comparative work.

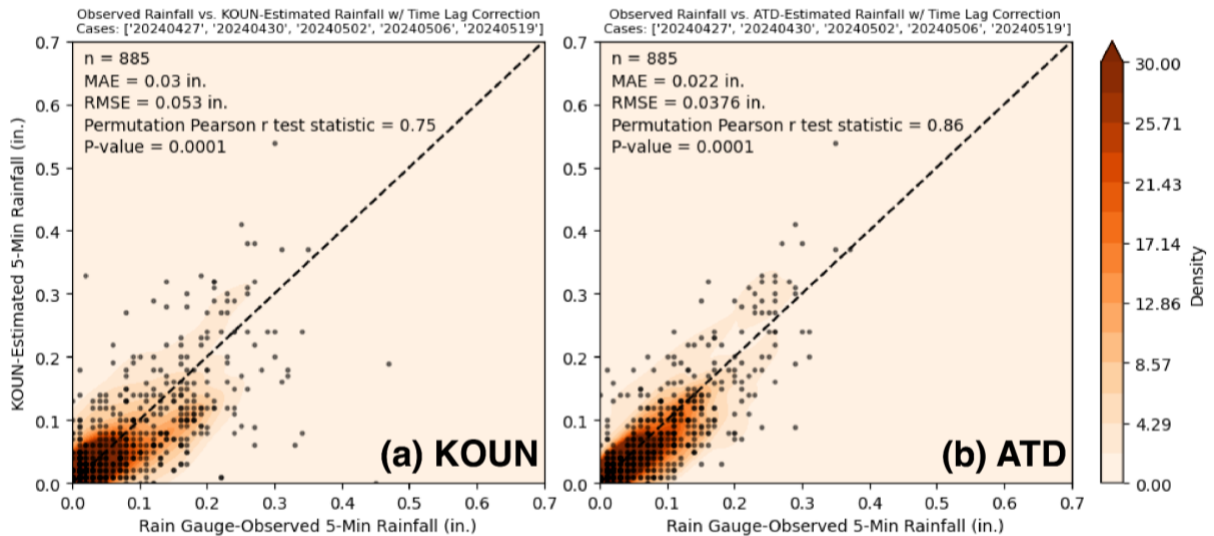


Figure 12. Composite radar-based QPE retrievals (y-axes) from (a) KOUN and (b) ATD are compared to 5-minute rain gauge observations (x-axes). The dashed one-to-one line indicates perfect agreement. The dots indicate observation comparison points and the color-filled contours indicate the density of those points according to the colorbar. In (a), KOUN QPE versus gauge-observed rainfall points are shown scattered around the one-to-one line with substantial spread, particularly above 0.1 inches. Comparatively, the ATD versus gauge observations in (b) are much less scattered and are more concentrated along the one-to-one line, particularly for higher rainfall measurements. The inset text in the figures indicates that each radar observed 885 individual 5-minute increments over the five cases sampled. KOUN and ATD QPE retrievals had mean absolute errors of 0.03 and 0.02 inches, RMSEs of 0.053 and 0.0376 inches, and permutation Pearson r test statistics of 0.75 and 0.86 (both statistically significant with p -values of 0.0001), respectively. The statistics support that the ATD performed better in terms of QPE for the five cases contributing to this composite analysis.

5.3 Dual-Polarization Measurements

As noted in section 3.1.2, the ATD was occasionally operated using LDR mode in CY24. LDR can provide additional polarimetric information with which to estimate hail size. To our knowledge, no dual-polarization S-band PAR system has ever been used to collect LDR data. As such, the potential benefits of LDR on a PAR system are only just beginning to be explored with the ATD.

LDR mode was employed in various datasets throughout CY24 including its first use in the 27 March 2024 (see Appendix 1) winter precipitation case in central Oklahoma. However, its utility was well demonstrated on 24-25 September 2024 when the ATD observed a hail-producing thunderstorm that began in the northern Oklahoma City metropolitan area and moved southeast past the ATD. During the collection, a low-level 0.5° elevation LDR scan immediately preceded a “traditional” dual-polarization PPI-based volume scan such that 0.5° elevation LDR and dual-polarization PPIs were captured

about 6 seconds apart. An example is shown in Figure 13, where traditional dual-polarization data (except K_{DP}) are shown at 2334:01 UTC alongside a corresponding LDR scan that was taken approximately 6 seconds prior. Within the PPI of reflectivity, three local maxima are seen, which all are in a region of negative Z_{DR} . The negative Z_{DR} region is very likely partially the result of differential attenuation. The corresponding LDR values in Figure 13 are generally near -15 dB, with smaller regions approaching -12 to -10 dB. These local maxima in LDR are generally not directly collocated with the individual reflectivity cores, suggesting that LDR offers some independent information for identifying regions of large hail.

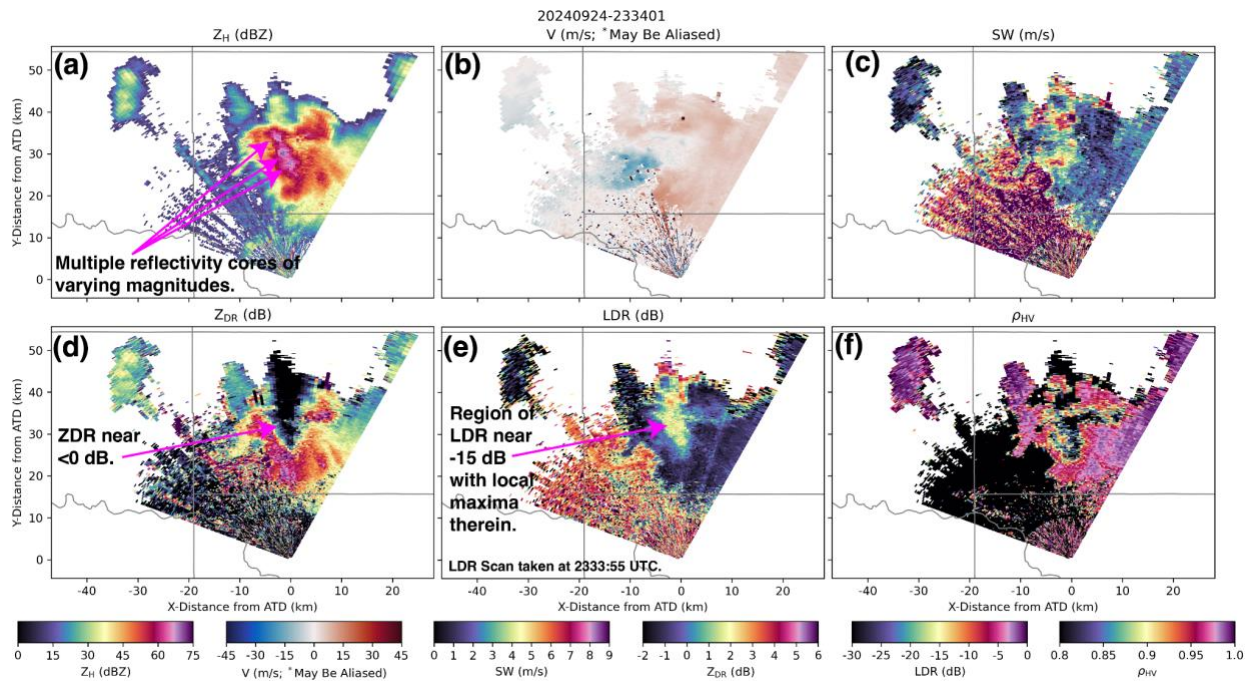


Figure 13. Dual-polarization data from the 24 September 2334:01 UTC PPI is shown, highlighting hail signatures in a severe storm to the northeast of the ATD. From top left to bottom right, panels of (a) radar reflectivity, (b) Doppler velocity), (c) SW, (d) Z_{DR} , (e) LDR (taken at 2333:55 UTC), and (f) ρ_{HV} are shown. Several distinct reflectivity maxima are indicated in (a) with values upwards of 65 dBZ. In the Z_{DR} field (d), a region of near or less than 0 dB is indicated that is very likely associated with a region of hail as well as differential attenuation. The same region is highlighted in LDR (e), which shows values near -15 dB (suggesting the presence of hail), with small isolated regions approaching -12 dB. The independent information gained from LDR likely adds value and context to the “standard” dual-polarization observations in terms of evaluating hail size, as discussed in the text.

Further analysis on this particular storm was performed to investigate the observed relationship between hail size and LDR versus reflectivity. Reports of hail size at the surface were collected as a function of time along with a time series of reflectivity and LDR in Figure 14. Between 2300 and 2315 UTC, a maximum in Z and LDR can be seen, which corresponds to the maximum *reported* hail size of the event. The second largest

hail was reported near 2345 UTC, corresponding to another peak in Z and LDR. However, the peaks (90th percentiles) in Z are quite similar between the times, whereas the peak in LDR is larger in the earlier case and smaller in the latter. As such, LDR seems to better capture the observed maximum hail size than Z as suggested by past idealized modeling studies (Mirkovic et al. 2022).

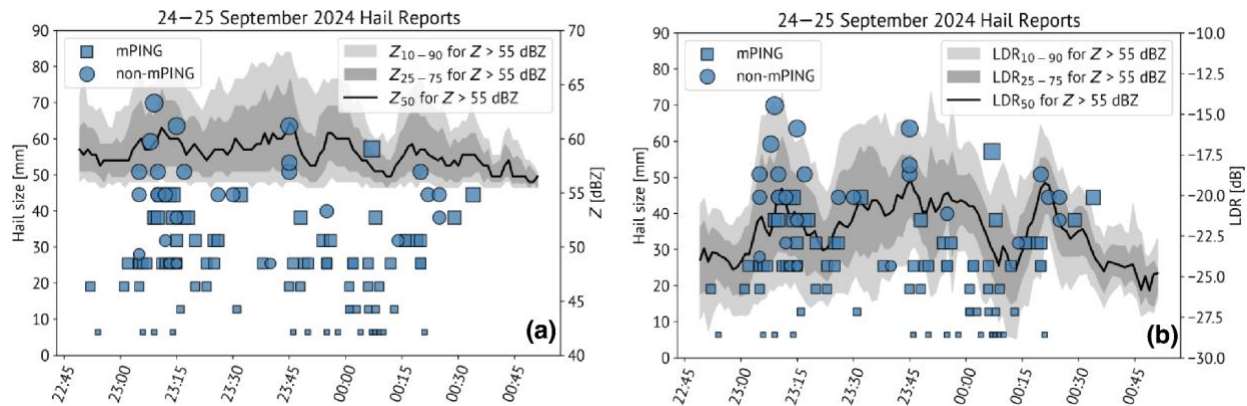


Figure 14. A time series for hail reports is compared to the ATD time series of (a) reflectivity and (b) LDR. The reflectivity and LDR time series are taken by only considering areas where reflectivity exceeded 55 dBZ. The black lines in each figure indicate the median value of reflectivity and LDR. The darker shading around the median line indicates the 25th to 75th percentile ranges. The lighter shading around the median indicates the 10th to 90th percentile ranges. The time series shows several peaks in reflectivity and LDR: a sharper peak near 23:07 UTC and a broader peak near 23:45 UTC. At those times, maximum hail sizes from reports were near 70 mm and 65 mm, respectively. The median, 75th, and 90th percentile values of reflectivity were near 60, 65, and 68 dBZ at both hail size peaks. However, LDR median, 75th, and 90th percentile values of LDR were near -20, -17.5, and -14 dB in the first peak and -19, -18, and -16 dB near the second peak, indicating utility in the independent information gleaned from LDR in hail sizing via radar observations.

5.4 Advanced Engineering Concepts

Finally, we briefly note areas in which NSSL meteorologists closely collaborated with engineers to facilitate the advancement of signal processing and engineering techniques being designed, tested, and implemented on the ATD.

5.4.1 Assisting with Calibration Efforts

As mentioned in section 3.1.3, weather scans were designed to calibrate spoiled transmit beams. To help facilitate the calibration efforts, NSSL meteorologists collected data in a mixture of convective and stratiform precipitation modes. In particular, collecting data during convective events presented an opportunity to examine the quality of spoiled

beam data when the spatial gradients in all measured radar variables are high. As spoiled beam scans are particularly useful for reducing scan times when observing rapidly evolving convection, some datasets where severe weather would normally be observed via pencil beam mode were conducted in a hybrid manner (i.e., both pencil and spoiled beam scans were conducted in succession as stated prior) for comparison as well as research and demonstration purposes. An example is shown in Figure 15. Multicellular convection observed on 5 July was targeted for data collection using alternating pencil and spoiled beams due to the strong spatial gradients, which present a challenge for spoiled beam scans. The spoiled transmit beams in this particular case were widened by a factor of 3 compared to pencil beams, which allowed the collection of data from 5 simultaneous azimuth angles for each radar transmission.

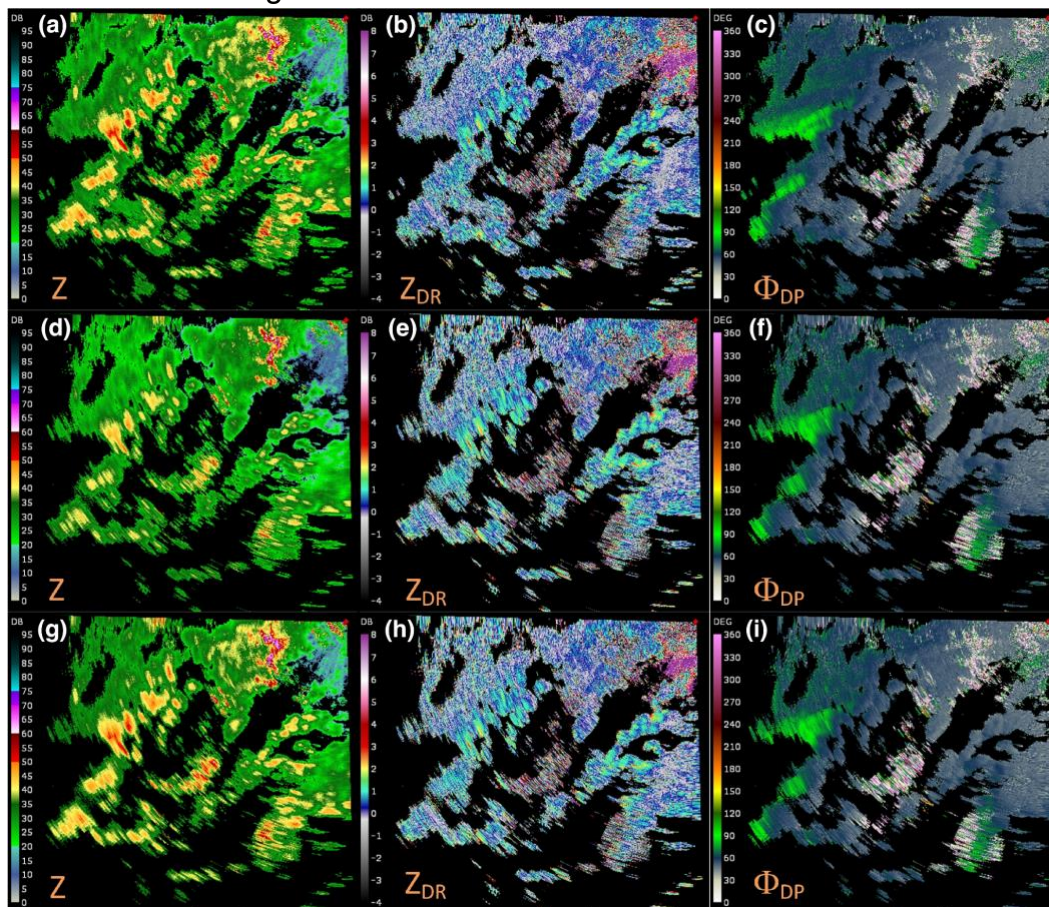


Figure 15. From left to right, fields of reflectivity, differential reflectivity, and differential phase for data collected with the ATD using pencil beams (a-c) and spoiled transmit beams with 5 simultaneous receive beams (d-i). Data in the (d-f) were calibrated using pre-existing correction factors derived for pencil beams only, while data in the (g-i) were calibrated using experimental weather data collected on 5 July 2024 1439:14 UTC.

The results demonstrate that the spoiled beam data can be calibrated (bottom row of Figure 15) using the combination of pencil and spoiled beam weather scans. A visual

evaluation of data fields in Figure 15 suggest the effects of non-calibrated spoiled beams are most noticeable in the reflectivity fields (i.e., comparison between the top and the middle leftmost panels visible), but is successfully accounted for using the weather-derived beamsteering bias correction factors (bottom left panels in Figure 15). The results in Figure 15 also demonstrate the expected loss of azimuthal resolution due to beam broadening (the pencil two-way beam at broadside is $\sim 1.6^\circ$ wide but increases to $\sim 2.2^\circ$ for spoiled beam used to collect data in Figure 15), as well as the discontinuities in data along azimuth (Figure 16). We are currently investigating if the irregular manner in which adjacent two-way beams overlap may contribute to this effect.

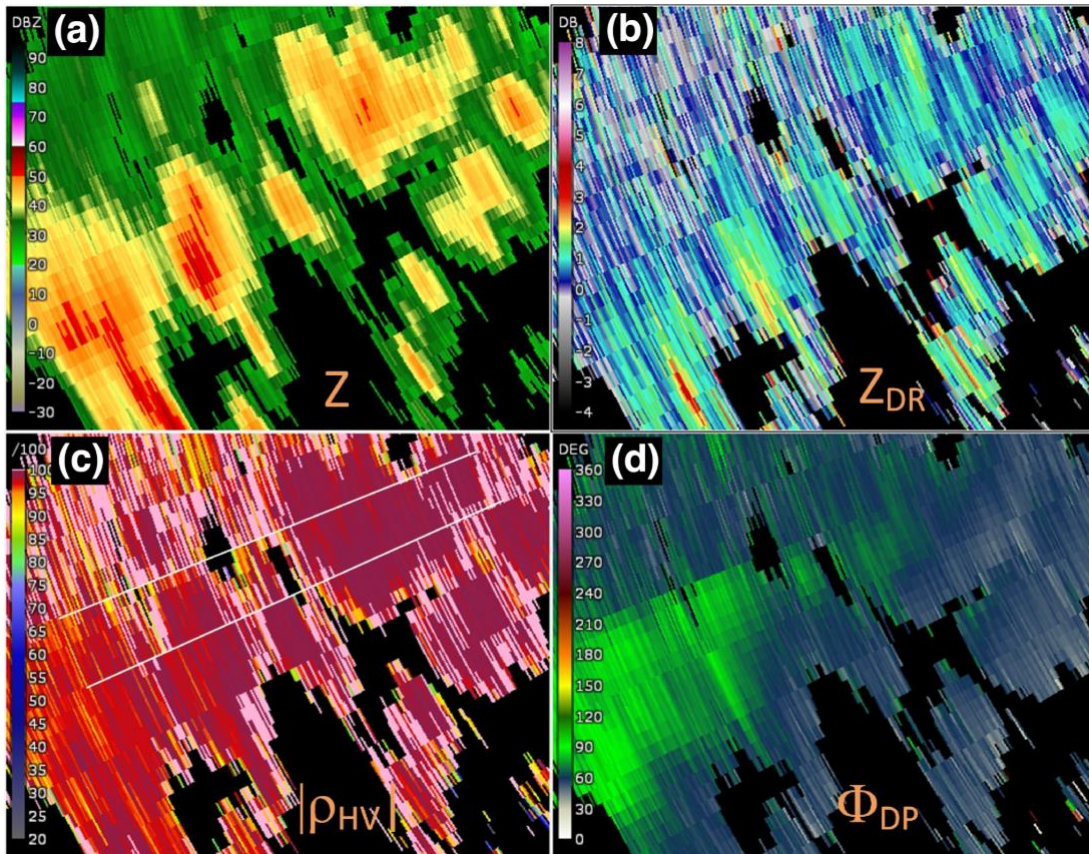


Figure 16. Magnified fields of reflectivity (a), differential reflectivity (b), correlation coefficient (c), and differential phase (d) from corrected spoiled beam data. The figure shows data collected by spoiled transmit beams to highlight the discontinuities discussed in the text. One group of simultaneously received beams is denoted between the white lines in (c).

5.4.2 Assisting with Adaptive Scanning R&D

Finally, as discussed in Section 2.1, adaptive scanning techniques were previously implemented on the SPY-1A PAR. The Adaptive Digital signal processing Algorithm for

Phased array radar Timely Scans (ADAPTS; Torres et al. 2016) was originally developed for the SPY-1A system, but a more advanced version is currently in development for implementation on the ATD. This version, referred to as ADAPTS V, is being tested on the ATD and incorporates dual-polarization data in order to determine beam positions with significant weather returns. Although it was still being refined and was not yet ready for full meteorological use in CY24, initial datasets have been collected by meteorologists so that the algorithm can be refined and fully implemented ahead of CY25.

Like in spoiled beam scanning, a variety of convective modes were targeted by meteorologists, particularly cases where convection was isolated or semi-isolated to test the ability of ADAPTS to select beam positions for observing rapidly-evolving convection. Several cases, such as the 30 October 2024 MCS case were considered hybrid collections. NSSL meteorologists employed scanning strategies that were research-focused, but the initial implementation of ADAPTS V was enabled simultaneously. Meteorologists operating the ATD carefully monitored the progress of the data collection to ensure that ADAPTS V was working as intended and did not unintentionally inhibit data collection (since ADAPTS V is still in active development).

6. Discussion

In CY24, the ATD observed a wide variety of severe and hazardous weather to advance the R&D goals of the NSSL PAR Program. This report has outlined several of the CY24 datasets collected by the ATD that help to advance the critical R&D efforts of the Program. Key areas covered include the operational demonstration and associated benefits of PAR, advancing NSSL's mission to further understand severe and hazardous weather, deepening the use and understanding of dual-polarization radar measurements, and developing advanced signal processing techniques and adaptive algorithms for current and future PAR systems.

6.1 Potential Operational Benefits Demonstrated by the ATD

As outlined in the CY23 report (Alford et al. 2024) and in this report, data collection with the ATD continues to support the premise that stationary PAR systems are capable of capturing rapid-update low-level and volumetric data. In section 5.1.1, we showed two example cases in which TDSs were observed earlier than by current operational systems. Theoretically, the earlier detection of rapidly evolving severe weather radar signatures can lead to earlier information dissemination to the public through, for example, severe weather warnings. We also showed that the rapid updates of such signatures can aid in confirming the temporal consistency of radar signatures that may be questionable at first glance. For example, with ~90-second, best-possible updates with the current WSR-88Ds, an initially "weak" or ambiguous TDS may result in uncertainty, which may require

waiting an additional ~90 seconds to establish the temporal consistency and assess the evolution of such a signature. However, with PAR data, it is possible to more quickly assess the evolution and temporal consistency of such signatures, which may lend additional confidence in earlier warning and/or forecast decisions.

In addition to low-level rapid updates, we also showed some of the benefits gleaned from rapid volumetric updates. In the examples shown, we examined how the structure and evolution of a rapidly evolving tornadic mesocyclone was better depicted by the ~1-minute ATD volumetric updates. In an operational setting, elevation angles sampled above 0.5° can provide insight into the intensity trends of the entire mesocyclone. In addition, vertical continuity of questionable signatures in the low levels may be interrogated by rapid-update volume data. We also examined the temporal trends of precursor K_{DP} cores near the freezing level in a severe, downburst-producing storm as an example of a precursor signature. In the case examined, the ATD not only captured the evolution of a strong K_{DP} core prior to severe winds occurring at the surface, but also depicted the evolution of two individual intensification periods. The comparative WSR-88D data was not able to resolve the fact that two K_{DP} intensification periods occurred. This observation is consistent with other datasets captured in CY24 and earlier in CY23 that indicate rapidly evolving mid- and upper-level features such as K_{DP} cores, hail growth and fallout, and mesocyclone trends rapidly fluctuating on timescales not observable by current operational systems.

The research efforts within the NSSL PAR Program also provide insight into the potential operational benefits of PAR. A critical question regarding PAR discussed in section 2.1 is the achievability of a quality dual-polarization calibration for a planar array PAR antenna. As mentioned, the ATD achieved a robust calibration in the early 2020s (Ivić et al. 2020, 2023). Although the quality of the calibration can be examined through self-consistency scans (e.g., section 5.4.1), additional examination of the calibration of the antenna can be gleaned from QPE retrievals. Shown in section 5.2.2., multiple CY24 datasets have been processed and directly compared to co-located and synchronous KOUN observations. The performance of QPE retrievals from the ATD are statistically better than KOUN observations for the composite analysis presented. The result is encouraging given that the ATD's beamwidth is wider than what will likely be expected of an operational system. In addition, the result confirms that the dual-polarization calibration is robust. The QPE method, the Multi-Radar Multi-Sensor QPE approach (Zhang et al. 2016) applied to a single-radar framework, employs a wide array of dual-polarization data and requires well-calibrated dual-polarization data. Current work on the subject continues to examine the case-by-case variability to identify if PAR may afford QPE improvements in varying convective modes (e.g., rapidly evolving convective events versus slowly varying stratiform events).

6.2 A Flexible and Adaptable Solution?

We also examined several examples that demonstrate PAR's ability to allow flexibility in scanning strategies and also adapt to the state of the atmosphere automatically. First, we showed an example of leveraging the ability of PAR to near-instantaneously change beam positions (without the need for mechanical motion) to collect high-resolution and very rapid (1 second) RHI scans. As shown in section 5.2.3, the only way to assess the vertical structure of convection via RHIs with current radars such as the WSR-88Ds is to reconstruct them from a traditional PPI-based volume scan. The same can be done via PAR PPI-based volume scans and offer improvement in the artificial tilt of radar features, for example, introduced by the long volume scan times of the WSR-88Ds. However, the ATD was used to show that fast, efficient, and high-resolution RHIs can be captured in about 1 second, which sacrifices a very small amount of time. If PAR were used as an operational technology in the future, a forecaster, an automated algorithm, or a combination thereof could direct RHIs to assess the vertical structure of much more than MCSs (e.g., hail cores, downbursts, mesocyclones).

An additional flexibility demonstrated by the ATD in CY24 was to incorporate LDR transmission into routine operations. In the example shown in section 5.3, a single LDR PPI scan (about 3-4 seconds to capture a single PPI scan) that followed a routine dual-polarization PPI scan can be used to interrogate additional information regarding hail size. LDR has much untapped potential in terms of incorporating the information gained from LDR into automated hail size algorithms and hydrometeor classification schemes as two examples. In addition, full PPI volumes of LDR information may be particularly useful in winter weather transition events where additional information is needed to separate regions of rain, freezing rain, ice pellets, and snow. As previously mentioned, LDR is much easier to incorporate into PAR-based scanning due to the use of electronic beam steering. On mechanical systems, LDR is generally not captured due to the time required to capture both LDR and dual-polarization data (with the latter prioritized). No doubt in CY24, the ATD has demonstrated that PAR can afford the ability to revisit LDR through flexible means of scanning at a small expense of time that may yield invaluable information to both forecasters and algorithms.

Finally, we noted the adaptability of PAR systems, which we illustrated through discussion of the ADAPTS V technique currently in development on the ATD. Algorithms like ADAPTS V can afford even faster revisits in the directions of significant echoes (e.g., a supercell occupying a subset of beam positions within the ATD's field of view) and deprioritize beam positions that are in directions free of significant weather returns. Future concepts of adaptive scanning may yield ways to adaptively scan different echo types (e.g., a smoke plume from a fire versus a tornado supercell) with scanning strategies tailored to each individual target of interest.

6.3 Moving into CY25

The concepts such as adaptive scanning, beam spoiling, and additional flexibilities in scanning that are being fully realized (in large part due to the R&D efforts in CY24) on the ATD system will be a top priority for data collection in CY25. In CY23, a key concept of scanning strategies was leveraging the ATD to examine the benefits of rapid ~1.5-minute updating scanning strategies that employed excellent vertical coverage (i.e., dense elevation angles/coverage). In CY24, ~1-minute volumes with redistributed and/or reduced vertical coverage with the flexibility of RHIs and LDR scans were examined. However, in CY25 the newly realized capabilities on the ATD will afford the ability to balance scanning strategies by leveraging the flexibility and adaptability of the ATD. By employing techniques such as adaptive focused observations, supercell scanning strategies can be designed for a “worst possible” update time of 1.2-1.5 minutes with good vertical coverage as a function of range and good data quality. However, the adaptive focused observations algorithm in most cases will likely reduce the total volume update (particularly for isolated supercells) by deactivating (but routinely re-checking) beam positions that do not require scanning, which will likely afford update times on the order of 1 minute or less. In addition, the use of beam spoiling (as the calibration of spoiled beams matures) throughout a volume scan will likewise be examined to determine how beam spoiling may be optimally employed to balance tradeoffs between update time, data quality, and coverage. We aim to also examine where in a volume scan (low versus mid versus upper elevation angles) beam spoiling may have the most positive impacts. Demonstrating an optimal combination of adaptive scanning techniques, pencil versus spoiled beam scanning, and flexible approaches to scanning will be a top priority of CY25.

7. Acknowledgements

The authors wish to acknowledge the support of the NSSL PAR Program, which supported the hardware and software development, data collection, and analysis outlined in this report. We also thank Dr. Kodi Berry, Dr. Ted Mansell, and Ms. Thea Sandmæl for their reviews of this report that improved its quality and content.

8. List of Acronyms

- AoA Analysis of Alternatives
- ADAPTS Adaptive Digital signal processing Algorithm for Phased array radar Timely Scans
- AFO Adaptive Focused Observations

- ATD Advanced Technology Demonstrator
- CY Calendar Year
- ρ_{HV} Correlation coefficient
- HMI Human Machine Interface
- HWT Hazardous Weather Testbed
- K_{DP} Specific differential phase (in units of degrees per kilometer)
- LDR Linear Depolarization Ratio
- MCS Mesoscale Convective System
- NOAA National Oceanic and Atmospheric Administration
- NSSL National Severe Storms Laboratory
- NWS National Weather Service
- PAMST Phased Array Meteorological Studies Team
- PPI Plan Position Indicator
- PRT Pulse Repetition Time
- QLCS Quasi-Linear Convective System
- RHI Range Height Indicator
- RMSE Root Mean Square Error
- SW Spectrum Width
- TDS Tornado Debris Signature
- VCP Volume Coverage Pattern
- WSR-88D Weather Surveillance Radar - 1988 Doppler
- Z Radar reflectivity (in units of dBZ unless otherwise specified)
- Z_{DR} Differential radar reflectivity (in units of dB)

9. References

Alford, A. A., and Coauthors, 2024: 2023 Data collection with the NSSL Advanced Technology Demonstrator. NOAA/NSSL Technical Memo, 47pp., doi: 10.25923/4v1r-yq31.

Ashley, W. S., A. M. Habberlie, and J. Strohm, 2019: A Climatology of Quasi-Linear Convective Systems and Their Hazards in the United States. *Wea. Forecasting*, **34**, 1605–1631, doi: 10.1175/WAF-D-19-0014.1.

Curtis, C. and S. Torres, 2011: Adaptive range oversampling to achieve faster scanning on the National Weather Radar Testbed Phased Array Radar. *J. Atmos. Oceanic Technol.*, **28**, 1581-1597, doi: 10.1175/JTECH-D-10-05042.1.

- Crum, T. D., and R. L. Alberty, 1993: The WSR-88D and the WSR-88D operational support facility. *Bull. Amer. Meteor. Soc.*, **74**, 1669–1688, doi: 10.1175/1520-0477(1993)074<1669:TWATWO>2.0.CO;2.
- Doviak, R. J., V. Bringi, A. V. Ryzhkov, A. Zahari, and D. Zrnica, 2000: Considerations for polarimetric upgrades to operational WSR-88D radars. *J. Atmos. Oceanic Technol.*, **17**, 257–278, doi: 10.1175/1520-0426(2000)017<0257:CFPUTO>2.0.CO;2.
- Heinselman, P. L., D. L. Priegnitz, K. L. Manross, T. M. Smith, and R. W. Adams, 2008: Rapid sampling of severe storms by the National Weather Radar Testbed Phased Array Radar. *Wea. Forecasting*, **23**, 808–824, doi:10.1175/2008WAF2007071.1.
- Heinselman, P. L., D. S. LaDue, and H. Lazrus, 2012: Exploring impacts of rapid-scan radar data on NWS warning decisions. *Wea. Forecasting*, **27**, 1031–1044, doi: 10.1175/WAF-D-11-00145.1.
- Heinselman, P. L., D. S. LaDue, D. M. Kingfield, and R. Hoffman, 2015: Tornado warning decisions using phased-array radar data. *Wea. Forecasting*, **30**, 57–78, doi: 10.1175/WAF-D-14-00042.1.
- Homeyer, C. R., T. N. Sandmæl, C. K. Potvin, and A. M. Murphy, 2020: Distinguishing Characteristics of Tornadic and Nontornadic Supercell Storms from Composite Mean Analyses of Radar Observations. *Mon. Wea. Rev.*, **148**, 5015–5040, <https://doi.org/10.1175/MWR-D-20-0136.1>.
- Ivić, I., R. Mendoza, D. Schwartzman, S. Torres, and D. Wasielewski, 2020: Preliminary report on polarimetric calibration for the Advanced Technology Demonstrator, NOAA/NSSL report, 34 pp. https://nssl.noaa.gov/publications/par_reports/.
- Ivić, I., F. Nai, and S. Torres, 2023: An update on polarimetric calibration for the Advanced Technology Demonstrator, NOAA/NSSL report, 74 pp. https://nssl.noaa.gov/publications/par_reports/.
- Ivić, I. 2024: An Overview of the PPAR Advanced Technology Demonstrator Polarimetric Calibration. ERAD 2024 Conference, Rome, Italy, doi: 10.13140/RG.2.2.23343.65442
- Ivić, I. 2025: PPAR Advanced Technology Demonstrator Polarimetric Calibration for Spoiled Beams. AMS Annual Meeting 2025, New Orleans, LA, doi: 10.13140/RG.2.2.21141.64485

- Kuster, C. M., B. R. Bowers, J. T. Carlin, T. J. Schuur, J. W. Brogden, R. Toomey, and A. Dean, 2021: Using KDP Cores as a Downburst Precursor Signature. *Wea. Forecasting*, **36**, 1183–1198, doi: 10.1175/WAF-D-21-0005.1.
- Kuster, C. M., K. D. Sherburn, V. N. Mahale, T. J. Schuur, O. F. McCauley, and J. S. Schaumann, 2024: Radar Signatures Associated with Quasi-Linear Convective System Mesovortices. *Wea. Forecasting*, **39**, 1143–1161, doi: 10.1175/WAF-D-23-0144.1.
- Kumjian, M. R., D. M. Tobin, M. Ou, and P. Kollias, 2020: Microphysical insights into ice pellet formation revealed by fully polarimetric Ka-Band Doppler radar. *J. Appl. Meteor. Climatol.*, **59**, 1557–1580, doi: 10.1175/JAMC-D-20-0054.1.
- Melnikov, V., D. S. Zrnić, M. E. Weber, A. O. Fierro, and D. R. MacGorman, 2019: Electrified Cloud Areas Observed in the SHV and LDR Radar Modes. *J. Atmos. Oceanic Technol.*, **36**, 151–159, doi: 10.1175/JTECH-D-18-0022.1.
- Mirkovic, D., D. S. Zrnić, V. Melnikov, and P. Zhang, 2022: Effects of rough hail scattering on polarimetric variables. *IEEE Trans. Geosci. Remote Sens.*, **60**, 2001314.
- Newman, J. F., and P. L. Heinselman, 2012: Evolution of a Quasi-Linear Convective System Sampled by Phased Array Radar. *Mon. Wea. Rev.*, **140**, 3467–3486, doi: 10.1175/MWR-D-12-00003.1.
- NOAA, 2024: Radar Next. https://www.noaa.gov/sites/default/files/2024-01/NOAA_Radar_Next-Radar_Next_Program_242901.pdf
- Schvartzman, D., S. M. Torres, and T.-Y. Yu, 2021: “Distributed beams: Concept of operations for polarimetric rotating phased array radar,” *IEEE Trans. Geosci. Remote Sens.*, **59**, 9173 - 9191, doi: 10.1109/TGRS.2020.3047090.
- Stratman, D. R., N. Yussouf, Y. Jung, T. A. Supinie, M. Xue, P. S. Skinner, and B. J. Putnam, 2020: Optimal temporal frequency of NSSL phased-array radar observations for an experimental warn-on-forecast system. *Wea. Forecasting*, **35**, 193–214, doi: 10.1175/WAF-D-19-0165.1.
- Torres, S. M., and Coauthors, 2016: Adaptive-weather-surveillance and multifunction capabilities of the National Weather Radar Testbed phased array radar. *Proc. IEEE*, **104**, 660–672, doi: 10.1109/JPROC.2015.2484288.

Torres, S. M. and D. Wasielewski, 2022: The Advanced Technology Demonstrator at the National Severe Storms Laboratory: Challenges and successes. IEEE Radar Conference, New York City, NY, IEEE, 1-6, doi: 10.1109/RadarConf2248738.2022.9764231.

Zhang, J., and Coauthors, 2016: Multi-Radar Multi-Sensor (MRMS) Quantitative Precipitation Estimation: Initial Operating Capabilities. *Bull. Amer. Meteor. Soc.*, **97**, 621–638, doi: 10.1175/BAMS-D-14-00174.1.

Zrnić, D., and Coauthors, 2007: Agile-beam phased array radar for weather observations. *Bull. Amer. Meteor. Soc.*, **88**, 1753–1766, doi: 10.1175/BAMS-88-11-1753.

Appendix 1: List of Case Details

Table 2. A list of all cases is shown with the case times and the general storm type observed. The fourth through eighth columns show the scan (VCP) date and time, the name of the scan, the ATD sector date and time, and the left (L) and right (R) edges of the ATD's sector. The information in these columns is color-coded according to changes in the VCP and sorted by time according to changes in the scanning strategy.

Date	Case Time (UTC)	Storm Type	VCP Date and Time	VCP Name	Sector Date and Time	L (°)	R (°)
1/5	10:39 – 12:01	Winter	1/5 10:39 1/5 10:44	ATD TPRT Demo WinterWx Shallow	1/5 10:39	295	25
1/14	15:02 – 19:30	Winter	1/14 15:02 1/14 18:54	WinterWx Deep WinterWx RHI Narrow	1/14 15:02 1/14 17:59 1/14 18:54	225 255 70	315 345 90
2/3	03:09 - 05:20	MCS (QLCS)	2/3 03:09 2/3 03:53 2/3 04:49	QLCS_100_Fast QLCS_75-100_Fast QLCS_50-75_Fast	2/3 03:09 2/3 03:44 2/3 04:12 2/3 04:46 2/3 05:03	185 175 165 150 135	275 265 255 240 225

Date	Case Time (UTC)	Storm Type	VCP Date and Time	VCP Name	Sector Date and Time	L (°)	R (°)
2/27 - 2/28	22:11 - 22:26, 00:32 - 01:13	Clear Air/Eng	2/27 22:11	Fire_Wx	2/27 22:11 2/28 00:32	255 290	345 20
3/7 - 3/8	01:23 - 01:44 and 02:43 - 03:13	Non-severe multicell	3/8 01:23 3/8 02:43	QLCS_75-100_Fast QLCS_50_Fast	3/8 01:23 3/8 02:43	295 235	25 325
3/14 - 3/15	15:34 - 18:11, 18:40 - 22:08, 23:06 - 00:42	Tornadic supercell	3/14 15:34 3/14 16:06 3/14 23:06 3/14 23:12	Supercell_100km_Fast Supercell_50km_to_100km Supercell_50-100km_Fast Supercell_100km_Fast	3/14 15:34 3/14 16:05 3/14 17:17 3/14 18:07 3/14 18:40 3/14 23:06	245 122 112 97 92 90	155 207 197 182 177 170
3/24 - 3/25	19:15 - 00:39	Severe multicells	3 19:20 3 20:22 3/25 00:22	QLCS_75-100_Fast Supercell_100km_Fast Supercell_50to100km_Fast	3 19:20 3 20:12 3 20:18 3 22:20 3/25 00:07 3/25 00:18 3/25 00:22	255 270 225 255 270 294 190 180	345 360 315 345 360 24 280 270
3/27	18:14 - 21:14	Winter	3/27 18:14 3/27 18:20 3/27 20:05	WinterWx Deep Playlist: WinterWx LDR (LDR WinterWx Test & LDR WinterWx ZDR Option) Added WinterWxRHI and WinterWxRHI LDR to playlist.	3/27 18:14 3/27 20:35 3/27 21:03	270 265 270	360 355 360
4/18	20:35 - 21:48	Non-severe multicell	4/18 20:35	CI Playlist (Fire Wx and RHISparse)	4/18 20:36	85	175
4/26	20:44 - 23:50	Non-severe multicell	4/26 20:52	Playlist: PAMST Supercell 100 km RHI fast	4/26 20:53 4/26 21:32 4/26 22:23 4/26 22:43 4/26 22:53 4/26 23:30 4/26 23:40	85 95 100 105 100 117 90	175 185 190 195 190 207 180

4/27 - 4/28	18:00 - 03:24	Tornadic supercell	4/27 18:01	Playlist: PAMST Supercell 100+km and RHI Fast	4/27 18:01	180	270		
					4/27 18:13	183	273		
					4/27 18:33	185	275		
					4/27 18:42	188	278		
					4/27 18:47	189	289		
					4/27 18:52	192	282		
					4/27 18:58	193	283		
					4/27 18:59	195	285		
					4/27 19:05	185	275		
					4/27 19:56	195	285		
					4/27 19:59	200	290		
					4/27 20:18	210	300		
					4/27 20:41	230	320		
					4/27 20:42	232	322		
					4/27 20:46	235	325		
					4/27 20:57	237	327		
					4/27 21:00	239	329		
					4/27 21:01	PAMST Supercell50to100km and RHI Fast	4/27 21:09	241	331
							4/27 21:13	243	333
							4/27 21:17	245	335
							4/27 21:20	247	337
							4/27 21:22	251	341
							4/27 21:26	253	343
							4/27 21:29	257	347
							4/27 21:32	259	349
							4/27 21:35	261	351
							4/27 21:37	263	353
							4/27 21:39	265	355
							4/27 21:42	268	358
							4/27 21:44	270	360
							4/27 21:47	272	2
							4/27 21:49	276	6
				4/27 21:53	278	8			
				4/27 21:55	280	10			
				4/27 21:56	282	12			
				4/27 22:00	284	14			
			4/27 22:23	Playlist: PAMST Supercell 100+km and RHI Fast	4/27 23:01	180	270		
			4/28 01:12	Playlist: PAMST Supercell 50-100km and RHI Fast	4/28 02:00	169	259		
			4/28 02:02	Supercell_0to50km_Fast	4/28 02:03	167	257		
					4/28 02:09	173	263		
					4/28 02:10	167	257		
					4/28 02:53	345	75		
					4/27 23:49	175	265		
					4/28 00:43	170	260		
					4/28 00:48	168	258		
					4/28 01:03	166	256		

					4/28 01:14	164	254
					4/28 01:20	167	257
					4/28 01:38	169	259
					4/28 01:50	171	261
			4/30 03:24	Playlist: PAMST QLCS_50to75km and RHI Fast	4/28 03:24	90	180

Date	Case Time (UTC)	Storm Type	VCP Date and Time	VCP Name	Sector Date and Time	L (°)	R (°)
4/30 - 5/1	21:06 - 03:56	Tornadic supercell	4/30 21:06	Playlist: PAMST Supercell_100km_Fast	4/30 21:06	215	305
					4/30 21:31	225	315
					4/30 22:01	227	317
					4/30 22:29	256	346
					4/30 23:07	212	302
					4/30 00:42	214	304
					4/30 00:47	210	300
					4/30 00:05	208	298
					5/1 00:24	210	300
					5/1 00:43	208	298
					5/1 00:50	206	296
					5/1 01:02	205	295
					5/1 01:21	287	197
					5/1 01:35	199	289
					5/1 01:44	200	290
					5/1 01:53	201	291
					5/1 01:58	202	292
5/1 02:05	204	294					
5/1 03:11	185	275					
5/1 03:16	182	272					
5/2	03:46 - 06:56	MCS (QLCS)	5/2 03:46	QLCS_100+km and RHI Fast	5/2 03:46	180	270
					5/2 04:02	189	279
					5/2 04:52	199	289
					5/2 05:22	192	282
					5/2 05:49	180	270
					5/2 05:52		
					5/2 06:01		
					5/2 06:12		
19:44 - 21:28			5/2 19:44	PAMST QLCS_100+km_and_RHI_Fast	5/2 19:44	225	335
					5/2 19:55		
					5/2 19:57		
					5/2 21:09		

5/6 - 5/7	19:41 - 04:56	Tornadic supercell	5/6 19:41	Playlist: PAMST Supercell 100+km and RHI Fast	5/6 19:41	225	335
					5/6 20:26	251	341
					5/6 20:28	253	343
					5/6 20:34	243	333
					5/6 22:01	247	337
					5/6 22:07	249	339
					5/6 22:13	251	341
					5/6 22:21	253	343
					5/6 22:28	255	345
					5/6 22:37	257	347
					5/6 22:45	259	349
					5/6 22:51	261	351
					5/6 22:58	263	353
					5/6 23:05	265	355
					5/6 23:11	267	357
					5/6 23:16	269	359
					5/6 23:21	271	1
					5/6 23:29	273	3
					5/6 23:34	275	5
					5/6 23:38	277	7
					5/6 23:43	279	9
					5/6 23:53	281	11
					5/6 23:55	283	13
					5/7 00:01	285	15
					5/7 00:04	287	17
					5/7 00:08	289	19
					5/7 00:13	291	21
					5/7 00:19	293	23
					5/7 00:25	295	25
					5/7 00:31	297	27
					5/7 00:35	299	29
					5/7 00:39	301	31
		5/7 00:42	303	33			
		5/7 00:46	305	35			
		5/7 00:49	307	37			
		5/7 00:53	309	39			
		5/7 00:59	311	41			
		5/7 01:03	313	43			
		5/7 01:06	315	45			
		5/7 01:09	317	47			
		5/7 01:12	319	49			
		5/7 01:16	341	251			
		5/7 01:22	343	253			
		5/7 01:26	270	0			
		5/7 01:33	272	2			
		5/7 02:02	278	8			
		5/7 02:05	Playlist: PAMST Supercell 50-100 km and RHI Fast	5/7 02:13	265	355	
				5/7 02:20	267	357	

					5/7 02:27	269	359
					5/7 02:31	260	350
					5/7 03:05	235	325
			5/7 03:07	Playlist: PAMST Supercell 100+km and RHI Fast			
			5/7 03:33	Playlist: PAMST Supercell 50 to 100 km Fast	5/7 03:52	225	315
					5/7 04:05	230	320
			5/7 04:09	Playlist: PAMST Supercell 0 to 50 km Fast	5/7 04:24	235	325
					5/7 04:35	245	335
					5/7 04:38	250	340
					5/7 04:41	260	350
					5/7 04:44	0	90
					5/7 04:47	335	65

Date	Case Time (UTC)	Storm Type	VCP Date and Time	VCP Name	Sector Date and Time	L (°)	R (°)
5/9	19:06 - 20:02	Severe multicell	5/9 19:06	PAMST Playlist Supercell 0-50km with Fast RHI	5/9 19:06	170	255
			5/9 19:08	LDR Playlist	5/9 19:08	165	255
					5/9 19:08	163	253
					5/9 19:11	160	250
					5/9 19:14	157	247
					5/9 19:28	150	240
					5/9 19:31	148	238
					5/9 19:32	146	236
					5/9 19:40	135	225
					5/9 19:42	115	205
					5/9 19:43	105	195
					5/9 19:44	100	190
					5/9 19:46	90	180
		5/9 19:47	84	174			
5/15	22:41 - 01:50	Severe multicell	5/15 23:43	Supercell_100km_Fast	5/15 23:44	304	24

Date	Case Time (UTC)	Storm Type	VCP Date and Time	VCP Name	Sector Date and Time	L (°)	R (°)
5/19	23:41 - 03:46	Tornadic supercell	5/19 23:41	Supercell_100km_Fast	5/19 23:41	245	335
			5/20 00:18	PAMST Supercell 100+km and RHI Fast	5/20 00:18	247	337
			5/20 00:28	Supercell 100+km Fast with SHV+AHV RHIs	5/20 00:37	245	335
					5/20 00:42	247	337
					5/20 00:53	249	339
					5/20 01:31	253	343
					5/20 01:37	257	347
			5/20 01:47	Supercell_50to100km_Fast	5/20 02:07	259	349
			5/20 02:07	Supercell 50_to_100km Fast with SHV+AHV RHIs			
			5/20 02:28	PAMST Supercell_0-50km and RHI_Fast	5/20 02:28	263	353
					5/20 02:52	270	360
					5/20 03:01	272	2
					5/20 03:03	274	4
					5/20 03:06	280	10
					5/20 03:07	282	12
					5/20 03:08	284	14
					5/20 03:10	288	18
					5/20 03:13	292	22
					5/20 03:17	296	26
					5/20 03:21	300	30
		5/20 03:23	300	30			
		5/20 03:23	302	32			
		5/20 03:27	304	34			
		5/20 03:29	310	40			
		5/20 03:32	318	48			
		5/20 03:40	324	54			
5/22	11:27 - 15:26	Eng Test	5/22 11:27	Table: Spoiled Beam Weather Engineering	5/22 11:27	280	10
					5/22 12:38	90	180
					5/22 14:24	90	180
5/22	17:37 - 19:19	Severe multicell	5/22 17:37	Supercell_100km_Fast	5/22 17:37	90	180
			5/22 18:01	Playlist Supercell 100 and RHI Fast	5/22 18:01	84	174

Date	Case Time (UTC)	Storm Type	VCP Date and Time	VCP Name	Sector Date and Time	L (°)	R (°)		
5/23	21:46 - 04:23	Tornadic supercell	5/23 21:48	Scan: Hail_150_200_Narrow	5/23 21:46	213	303		
					5/23 22:13	215	305		
					5/23 22:39	219	309		
					5/23 22:57	223	313		
					5/23 23:17	217	307		
					5/23 23:35	213	303		
					5/23 23:48	209	299		
					5/24 00:16	205	295		
					5/24 00:41	201	291		
			5/24 02:31	Playlist: PAMST LDR QLCS 100+km and RHI	5/24 02:35	203	293		
			5/24 03:23	Playlist: PAMST LDR Supercell 50-100km and RHI Fast	5/24 03:40	187	277		
					5/24 03:51	189	279		
					5/24 04:04	187	277		
					5/24 04:07	185	275		
					5/24 04:11	183	273		
5/24 04:12	181	271							
5/24 04:15	179	269							
5/24 04:16	177	267							
5/24 04:18	175	265							
5/25	21:02 - 01:19	Tornadic supercell	5/25 21:02	Supercell_100_fast	5/25 21:02	200	290		
					5/25 21:45	PAMST Supercell 100+km and RHI Fast	5/25 21:45	195	285
							5/25 21:57	196	286
			5/25 22:03	PAMST Supercell 50-100km and RHI Fast	5/25 22:03	200	290		
					5/25 22:07	207	297		
					5/25 22:10	205	295		
					5/25 22:17	203	293		
					5/25 22:42	265	355		
					5/25 22:43	255	345		
					5/25 22:47	259	349		
					5/25 22:50	263	353		
					5/25 22:55	265	355		
					5/25 22:58	269	359		
			5/25 23:07	275	5				
5/25 23:01	271	1							
5/25 23:19	280	10							
5/25 23:22	PAMST Supercell 100+km and RHI Fast								
5/25 23:35	Supercell_100km_Fast	5/26 01:05	290	20					

Date	Case Time (UTC)	Storm Type	VCP Date and Time	VCP Name	Sector Date and Time	L (°)	R (°)	
5/28	15:52 - 18:50	Severe multicell	5/28 15:52	Supercell 50-100 Fast	5/28 15:52	270	360	
			5/28 16:18	Supercell 100km Fast				
			5/28 17:25	PAMST Supercell 50-100 and RHI Fast Playlist	5/28 17:47	260	350	
					5/28 17:50	250	340	
					5/28 18:20	245	335	
				5/28 18:37	235	325		
				5/28 18:48	225	315		
5/30	16:59 - 18:55	Eng	5/30 16:59	Playlist: PAMST Self Consistency	5/30 16:59	180	270	
					5/30 17:41	105	195	
5/31	02:28 - 05:27	MCS	5/31 02:28	QLCS_100+km and RHI Fast	5/31 02:28	225	315	
					5/31 02:38	227	317	
					5/31 03:32	220	310	
					5/31 04:05	211	301	
					5/31 04:38	198	288	
6/3	18:20 - 18:55	Eng	6/3 18:20	PAMST Self Consistency Playlist	6/3 18:20	85	175	
			6/3 18:50	QLCS_75-100_Fast				
6/4	05:28 - 08:15	Severe multicell	6/4 05:28	Playlist: PAMST LDR Supercell_0-50km and RHI_Fast QLCS_50-75km_Fast PAMST QLCS_50-75 and RHI Fast	6/4 05:28	241	331	
					6/4 06:17	255	345	
					6/4 07:16	105	295	
					6/4 07:34	85	175	
6/5	00:07 - 05:15	MCS	6/5 00:07	PAMST LDR QLCS_0to50km and RHI Fast	6/5 00:07	265	355	
			6/5 00:09		6/5 00:09	271	361	
			6/5 00:36	PAMST LDR QLCS_75to100km and RHI Fast	6/5 00:36	183	273	
			6/5 00:54		6/5 00:54	224	314	
			6/5 01:19	PAMST QLCS LDR0.5 and QLCS_75to100	6/5 01:28	235	325	
			6/5 01:41	PAMST QLCS LDR0.5 and QLCS_50	6/5 02:23	135	225	
			6/5 02:54		6/5 02:54	100	190	
			6/5 02:52		6/5 02:52	90	180	
6/5 03:54	PAMST QLCS LDR0.5 and QLCS_75to100km	6/5 03:54	294	24				
6/5 04:32	PAMST QLCS LDR0.5 and QLCS_50to75km							

Date	Case Time (UTC)	Storm Type	VCP Date and Time	VCP Name	Sector Date and Time	L (°)	R (°)
6/20	18:30 - 18:46	Eng	6/20 18:30 6/20 18:40	Weather_Spoiled_Beam_Cal Playlist ART-Adv-ConOps Playlist	6/20 18:30	245	335
6/26	23:48 - 00:30	Eng	6/26 23:48	Playlist: Weather_Spoiled_Beam_Cal_Deg	6/26 23:48 6/27 00:05 6/27 00:19 6/27 00:27 6/27 00:33 6/27 00:38 6/27 00:44	180 225 135 155 175 195 215	270 315 225 245 265 285 305
6/29	22:01 - 02:17	Severe multicell	6/29 22:01 6/29 22:42	PAMST Supercell 100+km and RHI Fast PAMST Supercell 50-100km and RHI Fast	6/29 22:01 6/29 22:56	270 285	0 15
7/05	14:39 - 16:10	Eng	7/5 14:39 7/5 15:02 7/5 15:24 7/5 15:34	Playlist: Wx_Spoiled_Beam_Cal_Deg ART-Adv-ConOps Playlist: Wx_Spoiled_Beam_Cal PAMST Self-Consistency	7/5 14:39 7/5 15:14 7/5 15:28 7/5 15:34	180 305 225 180	270 215 315 270
7/7	15:34 - 17:08	MCS (QLCS)	7/7 15:34	Playlist: PAMST QLCS 100+ km and RHI Fast	7/7 15:34	90	180

Date	Case Time (UTC)	Storm Type	VCP Date and Time	VCP Name	Sector Date and Time	L (°)	R (°)
7/7 - 7/8	20:17 - 02:38	Severe multicell	7/7 20:17	PAMST QLCS_75to100km and RHI Fast	7/7 20:17	247	337
			7/7 20:23	PAMST QLCS_50to75km and RHI Fast			
			7/7 20:52	PAMST QLCS_0to50km and RHI Fast	7/7 21:15	239	329
					7/7 21:44	235	325
			7/7 21:48	PAMST Supercell_0-50km and RHI_Fast			
			7/7 21:58	PAMST LDR Supercell_0-50km and RHI_Fast			
			7/7 22:05	PAMST QLCS LDR0.5 and QLCS_50	7/7 22:44	215	305
					7/7 22:55	195	285
					7/7 23:32	170	260
					7/7 00:30	120	210
		7/8 00:47	PAMST QLCS LDR0.5 and QLCS_50to75				
		7/8 01:24	PAMST QLCS LDR0.5 and QLCS_75to100	7/8 01:54	135	225	
		7/8 01:55	PAMST QLCS LDR0.5 and QLCS_100				
8/15 - 8/16	21:31 - 01:15	Downburst	8/15 21:31	PAMST Downburst_75-100 and RHI Playlist	8/15 21:31	216	306
					8/15 22:24	254	344
					8/15 22:33	249	339
			8/15 22:49	PAMST Downburst_50-75 and RHI Playlist	8/15 22:49	249	339
		8/15 23:29	PAMST Downburst_50 and RHI	8/16 00:05	135	245	
9/24	22:45 - 00:58	Severe multicell	9/24 22:49	PAMST QLCS LDR0.5 and QLCS50	9/24 22:49	295	25
					9/24 23:36	305	35
					9/24 23:43	315	45
					9/24 23:50	325	55
					9/24 23:56	345	75
					9/24 00:03	5	95
					9/25 00:13	35	125
					9/25 00:23	65	155
					9/25 00:36	75	165
		9/25 00:40	90	180			
10/29	19:56 - 21:08	Clear Air	10/29 19:56	Fire_Wx	10/29 19:56	295	25

Date	Case Time (UTC)	Storm Type	VCP Date and Time	VCP Name	Sector Date and Time	L (°)	R (°)
10/30	19:24 - 03:00	MCS	10/30 19:25	Supercell_100km_Fast (Adaptive)	10/30 19:25	245	335
					10/30 20:26	260	350
					10/30 23:15	270	360
			10/31 00:11	Supercell_100km_Fast (3rd 0.5° Spoiled)	10/30 23:18	280	10
			10/31 01:55	Supercell_50to100km_Fast	10/31 01:39	225	315
		10/31 02:50	Table: Spoiled_Weather_FineRes				
11/2	18:41 - 05:47	MCS (QLCS)	11/2 18:41	PAMST QLCS_100+km and RHI Fast	11/2 18:41	188	278
			11/2 19:42	PAMST QLCS_50to75km and RHI Fast	11/2 19:42	225	315
			11/2 19:53	PAMST QLCS_0to50km and RHI Fast	11/2 20:11	188	278
					11/2 20:40	235	325
					11/2 21:16	285	375
			11/3 02:29	PAMST QLCS_75to100km and RHI Fast	11/3 02:29	192	282
			11/3 04:39	PAMST Supercell_0to50km and RHI Fast	11/3 04:39	85	175
		11/3 04:51	PAMST QLCS_100+km and RHI Fast	11/3 04:51	188	278	
11/3	19:39 - 23:24	MCS (QLCS)	11/3 19:47	PAMST: QLCS_100 and RHI Fast	11/3 19:47	180	270
					11/3 20:07	200	290
			11/3 20:33	PAMST: QLCS_75-100_Fast			
			11/3 21:20	PAMST: QLCS_50_Fast	11/3 21:07	215	305
					11/3 21:15	225	315
					11/3 21:29	230	320
					11/3 21:35	225	315
					11/3 22:50	90	180
		11/3 23:18	QLCS_100km_Fast				
		11/3 23:19	Table: Spoiled_Weather_FineRes				
11/4	12:34 - 13:10	MCS (QLCS)	11/4 12:34	QLCS_50_Fast	11/4 12:35	292	22
			11/4 12:48	Spoiled_Beam_Weather_FineRes			
			11/4 13:07	QLCS_50_Fast			

Date	Case Time (UTC)	Storm Type	VCP Date and Time	VCP Name	Sector Date and Time	L (°)	R (°)
11/4	16:22 - 21:19	Severe multicell	11/4 16:22	Supercell 0to50 km Fast	11/4 16:22	95	185
					11/4 16:28	90	180
					11/4 16:35	55	145
					11/4 16:54	45	135
			11/4 17:02	Supercell 50-100km Fast			
			11/4 17:43	Supercell_50to100_0.5Space	11/4 17:50	135	225
					11/4 17:51	115	205
			11/4 18:07	Supercell_50to100km_0.5Space (Adaptive Enabled)	11/4 18:13	95	185
					11/4 18:25	85	175
					11/4 19:23	65	155
				85	175		
			11/4 21:01	MRLE_Sim_0-to-50km			
			11/4 21:07	MRLE_and_SAILS_0-to-50km			
			11/4 21:14	Spoiled_Weather_FineRes			
11/8	17:23 - 21:38	Eng	11/8 17:23	Supercell_100km_Fast	11/8 17:23	225	315
			11/8 18:59	Spoil_Beam_Weather_Cal_LowElev			
			11/8 19:02	Spoil_Beam_Weather_Cal_HighElev			
			11/8 19:05	Spoiled_Beam_Weather_DegSpace_LowElev			
			11/8 19:11	Spoiled_Beam_Weather_DegSpace_HighElev			
			11/8 20:17	MRLE_Sim_0to50km	11/8 20:17	195	285
			11/8 20:18	Supercell_50to100km_0.5Space	11/8 20:56	185	275
					11/8 20:59	175	265
					11/8 21:02	165	255
					11/8 21:06	155	245
					11/8 21:11	100	190
					11/8 21:14	225	315
		11/8 21:14	Mid-tilt_SAILS				
		11/8 21:21	Raster_PPI_50-100km				
		11/8 21:28	Raster_PPI_Comparison				

Date	Case Time (UTC)	Storm Type	VCP Date and Time	VCP Name	Sector Date and Time	L (°)	R (°)	
11/18	04:50 - 17:04	MCS (QLCS)	11/18 04:47	Spoil_Beam_Weather_Cal_LowElev	11/18 04:50	225	325	
					11/18 05:20	180	270	
			11/18 05:36	Spoil_Beam_Weather_Cal_HighElev	11/18 06:10	90	180	
			11/18 06:29	Spoil_Beam_Weather_Cal_LowElev				
			11/18 06:54	Spoiled_Beam_Weather_DegSpace_LowElev				
			11/18 07:04	Spoiled_Beam_Weather_DegSpace_HighElev				
			11/18 07:10	Spoiled_Beam_Weather_DegSpace_ExElev				
			11/18 07:16	Spoiled_Beam_Weather_DegSpace_Position19_ExElev				
			11/18 07:25	Playlist: Raster_PPI_Comparison	11/18 07:25	190	280	
			11/18 08:08	Raster_PPI_150+km				
			11/18 08:28	MRLE_Sim_150+km				
			11/18 08:57	Playlist: PAMST QLCS_100+km and RHI Fast	11/18 08:59	205	295	
					11/18 09:58	220	310	
			11/18 11:06	Playlist: PAMST QLCS_75to100km and RHI Fast	11/18 11:25	235	325	
					11/18 12:00	240	330	
					11/18 12:06	254	335	
					11/18 12:11	250	340	
			11/18 12:12	Playlist: PAMST QLCS_0to50km and RHI Fast	11/18 12:16	255	345	
					11/18 12:24	260	350	
					11/18 12:31	265	355	
					11/18 12:36	270	0	
					11/18 12:46	275	5	
					11/18 12:50	280	10	
					11/18 12:54	285	15	
					11/18 13:04	290	20	
					11/18 13:56	90	180	
					11/18 14:15	Playlist: PAMST QLCS_75to100km and RHI Fast		
					11/18 15:14	Playlist: PAMST QLCS_100 and RHI Fast		
		11/18 15:33	Playlist: Spoil Beam Wx Cal Low El					
		11/18 16:19	Spoiled_Beam_Weather_DegSpace_LowElev					
		11/18 16:32	Table: Spoiled_Weather_FineRes					

Date	Case Time (UTC)	Storm Type	VCP Date and Time	VCP Name	Sector Date and Time	L (°)	R (°)
12/26		Eng	12/26 20:23 12/26 20:35 12/26 20:58 12/26 21:01 12/26 21:03 12/26 21:11 12/26 21:32	Spoil_Beam_Weather_Cal_HighElev Spoil_Beam_Weather_Cal_LowElev Spoiled_Beam_Weather_DegSpace_LowElev Spoiled_Beam_Weather_DegSpace_HighElev Spoiled_Weather_FineRes WinterWx LDR New-Testing Spoiled_Weather_FineRes	12/26 20:23	85	175